ACCEPTED MANUSCRIPT
Physics of Plasmas
This is the author's peer reviewed, accepted manuscript. However, the online version of record will be different from this version once it has been copyedited and typeset.
PLEASE CITE THIS ARTICLE AS DOI: 10.1063/1.5097143
AIP Publishing

Long-lived predator-prey dynamics in the pedestal of near-zero torque high performance DIII-D plasmas

K. Barada[1*], T. L. Rhodes[1], K. H. Burrell[2], L. Zeng[1], Xi Chen[2], M. E. Austin[3], L. Bardóczi[2], C.M. Muscatello[2], and W. A. Peebles[1]

[1]*Department of Physics and Astronomy, University of California, Los Angeles, California 90095, USA*
[2]*General Atomics, P.O. Box 85608, San Diego, California 92186-5608, USA*
[3]*University of Texas, Austin, Texas 78712, USA*

Abstract

Quiescent high performance plasmas (often termed QH-mode) are attractive due to the replacement of potentially damaging energy and particle releases known as edge localized modes (ELMs) by relatively benign edge harmonic oscillations (EHO). These EHOs are believed to be driven unstable by edge current and/or edge toroidal rotational shear and contribute to edge particle transport. Decreasing the applied neutral beam torque in standard QH- mode discharge leads to an improved quiescent phase of higher and wider pedestal, also known as the wide-pedestal QH-mode [Burrell *et al*, Phys. Plasmas 23, 05613 (2016)]. This work expands upon the observed limit cycle oscillation (LCO) dynamics [Barada *et al*, Phys. Rev. Lett 120, 135002 (2018)] in this wide pedestal QH-mode. The onset of these LCOs after wide-pedestal transition are found to be correlated with the disappearance of coherent EHOs which happens either when the edge maximum bootstrap current decreases after the transition or when the toroidal rotation is decreased consistent with simulation predictions. Sustainment of this quasistationary oscillating regime is found to be possible due to a predator-prey type competition between E×B velocity shear and turbulence density fluctuations facilitated by an inward propagation of non-zonal flow like toroidally and poloidally symmetric E×B velocity perturbations from these LCOs. These LCO dynamics are further controlled by adding electron cyclotron heating (ECH) to a neutral beam heated wide-pedestal QH-mode discharge which led to surprising increase in energy confinement correlated with a concomitant decrease in edge turbulence in contrast to normally observed confinement degradation in H-mode with ECH.

**E-mail: kbarada@physics.ucla.edu*

I. Introduction

The presence of a turbulence suppressed narrow edge region called the pedestal helps maintaining improved confinement in the core of a tokamak operated in high confinement or H-mode[1]. Normally in H-mode, the edge pedestal exhibits periodic perturbations called edge localized modes or ELMs[2] that lead to core confinement degradation as well as high radially outward particle and heat flux to the plasma facing components. These fluxes have the potential to decrease the lifetime of plasma facing components in future large tokamaks[3]. Successful suppression and mitigation[4] of these ELMs have been demonstrated in many tokamaks although there remains a challenge in suppressing these ELMs in a low plasma rotation H-mode discharge which is the planned expected mode of operation in international thermonuclear experimental reactor (ITER)[5]. Another option is to completely avoid ELMs by operating in an ELM-free H-mode regime. Quiescent H-mode or QH-mode[6-8] is one such ELM-free operational regime which normally needs high applied torque from neutral beam injection (NBI). Edge electromagnetic instabilities called the edge harmonic oscillations (EHO) have been shown[9] to contribute to the transport in these standard QH-mode plasmas and keep the pedestal gradients below the ELM-unstable limit. Recently[10], decreasing toroidal rotation (by using simultaneous co- and counter neutral beam injected torque) in a standard QH-mode resulted in spontaneous increase in both the pedestal width and height with the plasma transitioning to an even higher confinement state. The reason for this transition is not well understood but the improved state is thought to be maintained by changes in edge turbulence due to a bimodal change in the radial profile of $E \times B$ shear ($v'_{E\times B}$) in the edge plasma[10, 11]. This has been described as a decrease in the $v'_{E\times B}$ at the edge for $\rho \geq 0.91$ leading

Physics of Plasmas ACCEPTED MANUSCRIPT
This is the author's peer reviewed, accepted manuscript. However, the online version of record will be different from this version once it has been copyedited and typeset.
PLEASE CITE THIS ARTICLE AS DOI: 10.1063/1.5097143
AIP Publishing

to an increased amount of turbulence which is coincident with a decreased confinement and pedestal gradients in this region. Here ρ is a standard magnetic flux coordinate defined as the square root of the normalized toroidal flux. An increase in the $v'_{E\times B}$ for $\rho \leq 0.91$ leads to improved confinement and decreased turbulence levels which also correlates well with the increased pedestal height and width, i.e. the pedestal top has an apparent inward propagation. This regime of operation is known as the wide-pedestal QH-mode. Coherent EHOs are often observed to turn off just before the wide-pedestal transition but sometimes the EHOs come back stronger after the profile changes due to wide-pedestal transition.

The experimental set up and the main diagnostics used are described in Section II. Section III describes two discharges with similar neutral beam power and torque program but with different target densities which can show different EHO behavior after the wide-pedestal transition. Even if the EHOs return after wide-pedestal transition, they are suppressed at low enough applied beam toque. Within a few milliseconds after cessation of the EHOs, multiple transport relevant edge plasma parameters are observed to oscillate throughout the wide-pedestal operational regime which is limited by hardware constraints, i.e. NBI operational period. These oscillations and the changes in the edge radial profiles during these oscillations are described in section IV. Section V identifies the nature of these oscillations as limit cycle oscillations from the observations in phase-space plots of density turbulence , $v_{E\times B}$, and $v'_{E\times B}$ obtained from Doppler Backscattering (DBS) diagnostics. The relationship between $v'_{E\times B}$ and density turbulence (ñ) will be shown to have a predator-prey type behavior and in addition, the role of temperature gradient in the LCO process are also discussed in this section. A unique spatiotemporal variation of $v_{E\times B}$ leading to the $v'_{E\times B}$ temporal evolution is described in Section VI. Section VII identifies the nature of flow associated with the oscillations and outlines the differences between the LCO discussed in this work and those transiently observed during L-H transition[12-15]. Observation of confinement improvement and LCO period increase using additional ECH power in an NBI heated wide-pedestal QH-mode discharge will be discussed in Section VIII. Finally, the manuscript is summarized followed by future directions of research.

II. Experimental set up and key turbulence and flow diagnostics

The experiments reported here were performed in the DIII-D tokamak[16] which has major radius of ~1.74 m and minor radius of ~ 0.6 m. For the discharges described in this manuscript, a plasma current of ~1.1 MA and toroidal magnetic field of ~2.01 T. Neutral beams are used to change both power and injected torque. Co- and counter directed (to plasma current) neutral beam injection are used to ramp down the torque which leads to wide-pedestal transition. Plasma shaping is changed from upper single null to double null much before the start of the torque ramp down process.

Doppler backscattering (DBS) is the key diagnostics used to measure high time resolution turbulence and turbulence flow velocity. The DBS system[17] in DIII-D utilizes eight discrete probe frequencies in the range 55-75 GHz and is located near the vacuum midplane of DIII-D at toroidal angle, $\varphi \sim 60^{\circ}$. DBS is a relatively new measurement technique[17-24] that provides wavenumber and spatially resolved density fluctuation measurements as well as the flow velocity of these fluctuations. The local perpendicular flow velocity, $v_{\perp}$ is obtained from the Doppler shifted frequency $f_D = 2\pi k_{\perp} v_{\perp}$. Here $k_{\perp}$ is the perpendicular wavenumber of the density fluctuations which is dominantly in the poloidal direction near the cutoff location ($k_{\perp} \sim k_{\theta}$) and the total fluctuation velocity, $v_{\perp}$is composed of the local $E \times B$ velocity and turbulence phase velocity, i.e. $v_{\perp} = v_{E\times B} + v_{turb}$. With the measured Doppler shifted frequency and $k_{\perp}$ from 3D raytracing code GENRAY[25], $v_{\perp}$ can be estimated. Plasma frame linear TGLF[26] calculations[11, 27] performed in a similar discharge found that for the measurement locations and for fluctuations of interest here, the turbulence phase velocity in the plasma frame is much smaller than the measured turbulence flow velocities (v_{turb}< 1km/s compared to $v_{\perp}$~15-30 km/s). So, for the data presented here the turbulence flow is dominated by contribution from the local ExB velocity, $v_{\perp} = v_{E\times B}$. The intensity of the received DBS signal is proportional to $\tilde{n}^2$ and the rms value of ñ can be calculated by integration of the intensity over the Doppler shifted frequency range. $E \times B$ velocities measured by DBS at eight radial locations are used to calculate the $E \times B$ velocity shear and these will used to understand further the edge limit cycle dynamics in this manuscript. The plasma frame TGLF calculations[11, 27] also show modes propagating in

Physics of Plasmas ACCEPTED MANUSCRIPT
This is the author's peer reviewed, accepted manuscript. However, the online version of record will be different from this version once it has been copyedited and typeset.
PLEASE CITE THIS ARTICLE AS DOI: 10.1063/1.5097143
AIP Publishing

the electron diamagnetic drift direction in the range of measured intermediate-k ($k_\theta \rho_s \sim 0.8 - 1.8$, ρ_s is the ion Larmour radius with $T_e \sim T_i$) density fluctuations by DBS.

III. Evolution of coherent EHOs at wide-pedestal transition

In this section we investigate the underlying physics mechanism of coherent EHO behavior at the wide-pedestal transition. One interesting feature of these wide-pedestal QH-mode discharges is that often the EHOs turn off just before the transition and in some discharges the EHOs later reappear after the transition. Figure 1 shows two discharges which have different wide-pedestal transition times with different chord-averaged target electron densities but otherwise similar plasma parameters at least until the wide-pedestal transition. As the total injected beam torque is decreased, the discharge with higher target density displays a wide-pedestal transition around a time ~2395 ms (marked by black dot-dashed line in Figure 1) of the discharge. This is evidenced by both pedestal pressure height (Figure 1e) and width (Figure 1f) increasing when the input beam torque is approximately 2.9 Newton-meter (N-m). The EHOs return with stronger amplitude after ~ 40 ms of the transition as can be seen from the amplitude of toroidal mode number n=1 EHO amplitude in Figure 1c at ~2433 ms.

For the discharge with lower target density, the wide-pedestal transition occurs at a time ~2910 ms (shown by the red dot-dashed vertical line) when the beam torque is around 0.8 N-m. This value of NBI torque is much less than the value of 2.9 Nm for the higher target electron density case. In this lower target density shot, the EHOs do not return although the wide-pedestal is maintained for many energy confinement times.

The changes in radial profiles of electron pressure and its gradient before and after the wide-pedestal transition in these two discharges are compared in Figure 2. For both these discharges, the value of maximum pressure gradient and the pedestal top locations (see figure 2a and 2d) have moved radially inward after the transition. Also to be noted in both the discharges that the pressure gradient has decreased towards the lower half of the pedestal whereas it has increased towards the top of the pedestal. It can be seen that the maximum pressure gradient has increased (Figure 2b) after the wide-pedestal transition for the discharge in which the EHOs came back indicating height has increased more than the width. In contrast, the discharge in which the EHOs did not reappear shows a decrease in maximum pressure gradient (Figure 2e) after transition indicating increment in pedestal height is less than that of pedestal width after the transition as compared to before the transition in this discharge.

Calculations of edge bootstrap current in these two discharges are shown in Fig 2c and 2f, the maximum edge bootstrap current increases by ~20 % for the discharges in which the EHOs come back and decreases by ~30% for the discharge in which the EHOs never reappear. Simulations have shown that EHOs are consistent with peeling modes that are driven by edge current[28] (which has dominant contribution from the edge electron pressure gradient driven bootstrap current). The increase in pressure gradient can lead to higher edge bootstrap current which then can act as a stronger drive for the EHOs and this may explain why the EHOs come back strongly in the discharge with higher target electron density in which the maximum pressure gradient increased after the transition.

The appearance of strong oscillations in edge parameters after the disappearance of the EHOs is described next.

IV. Appearance of strong periodic oscillations after EHO cessation

In this section we describe the strong oscillations in edge parameters that appear after the cessation of the coherent EHOs. The variation of edge parameters, profiles and their gradients are examined. As the input beam torque is ramped down in the higher density discharge (shown in Figure 1) from ~2.5 Nm at 2433 ms to ~0.5 Nm at 3250 ms and kept constant after that at ~0.5 Nm, the EHO disappears at approximately 3257 ms indicated by decrease in EHO amplitude shown in Fig 1c and the magnetic spectrogram shows the EHOs disappear (not shown here). Within few (~2-3 ms) milliseconds after the EHO cessation, oscillations are observed in multiple transport relevant edge parameters as shown in Figure 3. These oscillations can be sustained for many electron energy confinement times [~3-28 τ_e] and are sustained for ~ 5 τ_e for the discharge shown in Figure 3. The wider and higher pedestal as well as the ELM-free state is maintained for many energy confinement times even in the absence of EHOs in more than 60 wide-pedestal QH-mode discharges studied, indicating that transport caused by the EHOs has been replaced by new transport mechanisms to sustain an ELM-free pedestal. In

Physics of Plasmas ACCEPTED MANUSCRIPT
This is the author's peer reviewed, accepted manuscript. However, the online version of record will be different from this version once it has been copyedited and typeset.
PLEASE CITE THIS ARTICLE AS DOI: 10.1063/1.5097143
AIP Publishing

fact, power balance calculations (not shown here) suggest no significant change in heat diffusivities going from the EHO phase to an EHO-free phase of the wide-pedestal QH-mode discharge[27].

Figure 3 shows oscillations in edge T_e measured by electron cyclotron emission (ECE) diagnostics at ρ~0.91 and C^{6+} ion temperature measured by charge exchange recombination (CER) spectroscopy (Fig 3a), Divertor Deuterium-alpha (D_α) radiation light intensity (Fig 3b) measured by filterscope, ion saturation current density measured by floor Langmuir probe (Fig 3c), and radial electric field measured by charge exchange recombination (CER) spectroscopy at ρ ~0.91(Fig 3d). As can be seen, each drop in edge T_e is associated with increases in D_α light intensity and Langmuir probe ion saturation current density (J_{sat}) and a decrease in edge radial electric field (E_r) magnitude. These data indicate that the underlying physics mechanism of these oscillations is strong enough to affect multiple and different edge parameters. Although these parameters are measured at different poloidal, toroidal, and radial locations, they oscillate at the same frequency (~54 Hz) and these oscillations will be identified as LCOs in the following section. The modulations in Langmuir probe ion saturation current density ($J_{sat} \propto n_e\sqrt{T_e}$) suggests modulated particle transport at LCO timescales. The divertor heat flux (not shown here) measured by infrared (IRTV) cameras also shows modulations at LCO frequency. For clarity and brevity these perturbations will be referred to as LCOs even though the demonstration of this will be deferred to the next section.

Not only the edge parameters but also the radial profiles of n_e and T_e measured by Thomson scattering diagnostics, and the pressure calculated from these above profiles also show appreciable changes during one LCO period. Figures 4 b-d show these profiles at two times (both within one LCO period) marked by the black (at 3325 ms) and red arrows (at 3339 ms) in Fig. 4a of electron temperature measured at ρ~0.91. Black and red curves in figures 4b-d correspond to profiles at times 3325 ms and 3339 ms respectively. As can be seen the height and width of the pressure pedestal is changing over one LCO period. Data obtained from high time resolution profile reflectometry measurements (shown in Figure 5) also show that the height and width of the density pedestal (calculated by tanh fitting of profiles) are oscillating at LCO timescales. The density pedestal width (shown in figure 5b) was found to be increasing more than the density pedestal height (shown in figure 5a) during LCO cycles (figure 5d) leading to a decrease in density pedestal gradient (shown in figure 5c). This behavior of decreased density pedestal gradient due to increase in the density pedestal width is very different from that reported during inter-ELM[29] periods of DIII-D H-mode discharges.

Confirming these changes also are the changes in gradients of electron density, temperature, and pressure (Figure 6a-6f) over time at two different radial locations (around pedestal top at ρ~0.87 and near maximum gradient region of the pedestal at ρ~0.94) calculated from high time resolution T_e and n_e measured by ECE and profile reflectometry diagnostics, respectively. Clearly, the pressure gradients are modulated at LCO time scales and it appears that the pressure gradient variations at the pedestal top follow the changes in pressure gradient at the mid-pedestal. After the pressure gradient in the steep gradient region drops (time indicated by vertical dotted lines in Fig 6e-f), the pressure gradient around the pedestal top also decreases but with a time delay. Due to similar trends of local T_e and n_e gradients during an LCO period, we will focus only on variations of ∇T_e. It was also found that gradients of electron and impurity ion pressure vary similarly during these LCO events. The relation between the oscillations in pedestal parameters, profiles, and profile gradients with other important transport relevant parameters like ñ, ∇T_e, $\upsilon_{E\times B}$ and $\upsilon'_{E\times B}$ and their mutual relationships during these LCO events will be discussed in the following section.

V. Coupled density turbulence ñ, velocity shear $\upsilon'_{E\times B}$, and gradient drives, limit cycle oscillations, and consistency with a predator-prey system

In this section the relationships between the parameters discussed above as well as local density turbulence ñ, velocity shear $\upsilon'_{E\times B}$, and gradient drives are examined. It will be shown that these form a coupled system exhibiting behavior consistent with a predator-prey system. To understand the pedestal dynamics associated with these long-lived oscillations of both edge parameters and profile gradients, ñ, $\upsilon_{E\times B}$, and $\upsilon'_{E\times B}$ are either measured or estimated from measurements using an eight channel Doppler backscattering[17] (DBS) diagnostics system described in section II.

Physics of Plasmas
ACCEPTED MANUSCRIPT
This is the author's peer reviewed, accepted manuscript. However, the online version of record will be different from this version once it has been copyedited and typeset.
PLEASE CITE THIS ARTICLE AS DOI: 10.1063/1.5097143
AIP Publishing

Figure 7a shows the density turbulence intensity spectrum measured by DBS at ρ~0.91 in a time window of ~50 ms, which is much after the EHO cessation time ~3257 ms in the higher target density discharge shown in Figure 1. This spectrum shows regular bursts in ñ intensity and associated with each of these turbulence bursts is a decrease in of the Doppler shifted frequency. Figure 7b-d compare ñ rms values, $v_{E\times B}$, ∇T_e, and velocity shear $v'_{E\times B}$. Figure 7b shows the ñ rms values calculated by integrating the intensity shown in figure 7a over a Doppler shifted frequency range of 800-4000 kHz. Figure 7c shows the $v_{E\times B}$ calculated using the information of Doppler shifted frequency and fluctuation wavenumber from GENRAY. ∇T_e at this location (Figure 7d) is calculated from ECE measurements and shows similar temporal behavior as that of $v_{E\times B}$. $v'_{E\times B}$ (Figure 7e) between consecutive probed locations is calculated from the already obtained $v_{E\times B}$ at eight probed radial locations and interpolated to the probed locations. As can be seen from figure 7b-e, ñ rms, $v_{E\times B}$, ∇T_e, and $v'_{E\times B}$ all show periodic behavior at the same frequency.

For ease of understanding, we have divided the oscillation period into three phases as indicated by red, blue, and black shades and also their individual durations are marked in Figure 7. Phase 1 corresponds to a time period in which ñ increases rapidly, phase 2 is the period of time when ñ decreases rapidly, and in phase 3, ñ increases slowly in time. In phase 1 as ñ rms increases, $v_{E\times B}$ and ∇T_e decrease while $E \times B$ shear is decreasing. In phase 2 as ñ is decreasing, $v_{E\times B}$ continues to decrease and increases later, ∇T_e continues to decrease and $E \times B$ shear increases first and when ñ is very low, $E \times B$ shear also decreases. In phase 3, ñ increases slowly, $v_{E\times B}$ and ∇T_e increase and saturate, and $E \times B$ shear increases slowly until the start of the next cycle.

Mutual relationships between these quantities are studied by their respective phase spaces in figure 8. Although only one cycle is shown in all the phase space plots for clarity, the individual values of respective parameters come back to the same values after each cycle as can be seen in Figure 7b-d confirming the limit cycle behavior. As timescales involved in these periodic phase space behavior match with that of quantities shown in figure 3, the oscillations in figure 3 are described as LCOs in section IV. Figure 8a shows the phase space of $v_{E\times B}$ vs ñ and displays an LCO type character. With the progression of time, a point on this curve moves in the clockwise direction with changes in $v_{E\times B}$ leading the changes in ñ e.g. a decrease in $v_{E\times B}$ in phase 1 is followed by a decrease in ñ in phase 2. When ñ increases, $v_{E\times B}$ decreases in phase 1 and later when ñ decreases, $v_{E\times B}$ also decreases in phase 2. In phase 3, both ñ and $v_{E\times B}$ increase slowly in time. ñ is known to affect $v_{E\times B}$ either increasing the value of $v_{E\times B}$ via zonal flow generation mechanism[30] or by decreasing it by reducing the profile gradients via turbulence transport. It is generally thought that $v_{E\times B}$ cannot directly affect ñ whereas flow shear, $v'_{E\times B}$ can affect the turbulence by shearing and decorrelating turbulent eddies[31], thus acting as a damping parameter on ñ.

Figure 8b shows the phase space of flow shear, $v'_{E\times B}$ vs ñ which also exhibits an LCO type behavior. For the sake of clarity, here also only one cycle is shown although the phase space nearly repeats itself for multiple cycles while oscillating in between high $v'_{E\times B}$/low ñ and low $v'_{E\times B}$ /high ñ states. With progression of time, a point on this curve moves in the counter-clockwise direction indicating $v'_{E\times B}$ is lagging ñ. In phase 1, as $v'_{E\times B}$ decreases (with increasing time), ñ increases significantly, by ~300%. In phase 2, as $v'_{E\times B}$ increases ñ reduces significantly (~85%). As phase 2 ends, the flow shear decreases significantly when ñ is very low. In phase 3, both $v'_{E\times B}$ and ñ increase slowly. This behavior appears to be consistent with a predator-prey type system often observed or simulated in ecological systems, e.g. the classic lynx/predator and hare/prey system[32]. Here, $v'_{E\times B}$ is consistent with being a predator while ñ acts as its prey i.e. when shear (predator population) decreases, ñ (prey population) increases, when shear (predator population) increases, ñ (prey population) decreases and when ñ (prey population) is very low then shear (predator population) also decreases. In the classic predator-prey system only two populations are posited, while here it will be seen that a more complex interaction involves a turbulence drive term interacting with both ñ and $v_{E\times B}$.

Plotted in Fig. 8c is the phase space of ∇T_e vs ñ showing limit cycle type behavior. For simplicity and consistency with the observation that local gradients of electron density and temperature are varying similarly (see Fig. 6a-d), only ∇T_e is used. Interestingly, a point in this phase space moves in a clockwise direction similar to the $v_{E\times B}$ vs ñ phase space. In phase 1, when ñ increases ∇T_e decreases. When ñ decreases, ∇T_e also decreases in phase 2. In

ACCEPTED MANUSCRIPT
Physics of Plasmas
This is the author's peer reviewed, accepted manuscript. However, the online version of record will be different from this version once it has been copyedited and typeset.
PLEASE CITE THIS ARTICLE AS DOI: 10.1063/1.5097143
AIP Publishing

phase 3, ∇T_e and ñ increase slowly. This slower and small increase of ñ in phase 3 can be explained by simultaneous increases in both ∇T_e and $v'_{E\times B}$ (Figure 8b-c) in this phase. As can be seen, the gradient changes during the maximum changes of ñ i.e. phase 1 and 2, are much smaller (percentage wise) compared to corresponding changes in $v'_{E\times B}$. This suggests a dominant role of $v'_{E\times B}$ over ∇T_e in regulating ñ with ∇T_e (or equivalently ∇P_e) providing a nearly constant drive for turbulence throughout the cycle. Furthermore, a point on the ∇T_e – ñ curve (Fig. 8c) rotates clockwise with time such that a predator-prey type picture indicates that ñ acts as a predator on the ∇T_e. This is consistent with turbulence driven transport (particle flux $\Gamma = \langle \tilde{n}\tilde{E}\rangle/B$ and convective thermal flux $Q_{e,conv} = 3/2\widetilde{\boldsymbol{T}_e}\Gamma$) driven by density fluctuations, ñ modifying the temperature profile and its gradient.

VI. Spatiotemporal dynamics and shear generation

The mechanisms underlying the velocity shear evolution are presented in this section. It will be shown that a spatiotemporal variation of the ExB flow velocity, $v_{E\times B}$ is key to understanding this system. Figure 9a,b show the temporal evolution of ñ and $v_{E\times B}$ at three different radii (only three radii chosen for simplicity). As multiple radial locations are considered and LCO phases are defined specific to a radial location, different notations are used to specify the times of interest as I, II, III, and IV and are indicated by vertical dashed lines.

ñ (Fig 9a) increases nearly at the same time at all radial locations but peaks at a later time (i.e. is delayed) as the measurement location moves inward. The $v_{E\times B}$ evolution shows a very interesting spatiotemporal behavior (Fig. 9b). As $v_{E\times B}$ starts to decrease at the outer radial location ρ~0.92 around time I, $v_{E\times B}$ at inner probed radial locations is seen to increase at this time. This results in a decreased difference between the $v_{E\times B}$ between these radial locations that in turn gives rise to a lower velocity shear $v'_{E\times B}$ (e.g. Fig. 9c of $v'_{E\times B}$ at ρ~0.90 in the time interval of I-II. This decrease in $v'_{E\times B}$ is coincident with an increase of ñ at this radius (Fig 9a). Later after time II, the drop in $v_{E\times B}$ at the outer radial location stops but $v_{E\times B}$ at inner radial locations continue to decrease in the time interval II-III, and this increase of difference in $v_{E\times B}$ values leads to an increase in $v'_{E\times B}$. This increase in $v'_{E\times B}$ is correlated with decrease of ñ at this location (Fig. 9c and 9a). Later, as $v_{E\times B}$ at the inner radial locations starts to increase to their original values as before time I, $v'_{E\times B}$ drops due to lesser difference in $v_{E\times B}$ while ñ remains roughly constant. Thereafter, $v'_{E\times B}$ and ñ increase slowly until the start of time I in the next LCO cycle and the process continues.

This spatiotemporal behavior of $v_{E\times B}$ is the key to understanding the dynamics of this predator-prey system. That is, the inward pulse like propagation of $v_{E\times B}$ reduction and the associated time delays at each radial location set up a spatiotemporally varying shear $v'_{E\times B}$ and ñ. Importantly, this system is seen to include inherently one or more spatial dimensions as well as time. This complex system is very different from the ideal predator-prey system described by Lotka-Volterra equations which describe the dynamics in a localized space without accounting for practical parameters like spatial diffusion[33-35] of predator and prey population in time.

A cartoon shown in Figure 10 summarizes the inferred dynamics from the above mentioned experimental observations of multifield predator-prey interactions. As can be seen from figure 10, ñ affects edge pressure gradients of both electron and ions. Changes in edge pressure gradients affect the edge radial electric field and $v_{E\times B}$. Spatiotemporal delay associated with $v_{E\times B}$ evolution creates the necessary $v'_{E\times B}$ which regulates ñ and the cycle repeats. In these low toroidal rotation plasmas, edge E_r and the resulting $v_{E\times B}$ have a dominant contribution from the diamagnetic (radial pressure gradient driven) force in the force balance equation[36] and it should be noted that all the charged species (electrons, main ions, and carbon ions) obey their own force balance equation and see the same radial electric field. This is confirmed by CER measurements of C^{6+} ions (shown in figure 11 at three different radial locations) which clearly show that the radial electric field has much more contribution from the diamagnetic pressure gradient of C^{6+} ions as compared to the rotation of C^{6+} in the pedestal. The pressure gradient of C^{6+} ions and total radial electric field (figure11c) are found to oscillate at the same LCO frequency as the pressure gradient (figure 6e-f) of electrons. Also, the phase spaces of ∇T_e vs ñ (figure 8c) and $v_{E\times B}$ vs ñ (figure 8a) are similar and both rotate in clockwise directions as time progresses. In our experiments, we found that electron pressure gradient varies almost linearly with C^{6+} ion pressure gradient during the LCOs.

Physics of Plasmas ACCEPTED MANUSCRIPT
This is the author's peer reviewed, accepted manuscript. However, the online version of record will be different from this version once it has been copyedited and typeset.
PLEASE CITE THIS ARTICLE AS DOI: 10.1063/1.5097143
AIP Publishing

These above observations indicate ñ affects both electron and ion pressure gradients via radial transport thus connecting the changes in ñ to that of edge $E \times B$ velocity and its shear. So, ∇T_e (or ∇P_e since ∇n_e changes are similar to ∇T_e, see fig 6) acts as a drive for ñ and evolution of ∇P_i induces changes in edge radial electric field, $v_{E\times B}$, and $E \times B$ shear in these low toroidal rotation plasmas.

It should be noted that high time resolution $E \times B$ velocities and their shear used in this manuscript are obtained from DBS measurements if not specified otherwise and not from CER measurements although they generally agree well. These observations present a coupled and complex predator-prey system of ñ, ∇T_e, $v_{E\times B}$, and $v'_{E\times B}$ in which changes in ñ affect ∇T_e and are affected by $v'_{E\times B}$, whose evolution depends on the spatiotemporal evolutions of $v_{E\times B}$. These dynamics are illustrated in Figure 10. The increase in density turbulence ñ has been found to be correlated with a decrease in edge ∇T_e (and also edge pressure gradient) in each LCO cycle as shown in Figure 8c. This can potentially keep the pedestal below the ELM-unstable limit via turbulence driven transport which is evidenced by the cyclic modulations of the Langmuir probe ion saturation current (Figure 3c) and other transport relevant edge parameters shown in Figure 3.

VII. Source of LCO flow perturbations: Zonal or mean $E \times B$ flow

The source of these low frequency LCO flow perturbations can be due to a variety of effects including poloidal and toroidal plasma flow, pressure gradients, zonal flow, etc. Zonal flows[30] are very low frequency toroidally and poloidally symmetric flows driven by turbulence anisotropy at higher turbulence levels whereas the mean $E \times B$ flow is driven by mean plasma rotation (toroidal and poloidal) and mean edge pressure gradient. The nature of the flow was investigated by simultaneously measuring $v_{E\times B}$ with two independent DBS systems toroidally separated by 180º and poloidally separated by ~ 9 cm (due to upward and downward probe beam launches relative to midplane) but at nearly the same radial location (same probe frequency). Figure 12 shows the cross-correlation between these toroidally separated $v_{E\times B}$ measurements for two different periods of the wide-pedestal QH-mode: one in EHO dominated phase and the other in LCO phase. As can be seen, the cross-correlation increases from ~0.1 to ~0.7 going from the EHO phase to the LCO phase of the wide-pedestal QH-mode. This strong correlation and low time lag (~0 ms) in the LCO phase is consistent with an $m \simeq 0$ and $n \simeq 0$ nature of the LCO flow perturbations (here m and n are the poloidal and toroidal mode numbers respectively). Despite possessing poloidal and toroidal symmetry, we found that these LCO flow perturbations are very different from the zonal flow dominated perturbations associated with the different, transient type of LCOs[12-15] reported from the L-H transition experiments. Figure 8a shows that when turbulence increases to its maximum value during the one limit cycle, flow decreases which is opposite to the behavior reported by the transient LCO L-H mode transition data[14]. In addition, the behavior shown in Fig. 8a seems contrary to that expected from zonal flow picture in which flow increases due to higher ñ generated turbulence Reynold's stress[15]. This data indicates that, although zonal flows may be present, any zonal flow contribution to the overall flow is subdominant to that of mean $E \times B$ flow which can be modified by turbulence driven radial transport.

VIII. Increased confinement and control of LCO using additional electron cyclotron heating

From the above it was found that ñ, ∇T_e, $v_{E\times B}$, and $v'_{E\times B}$ are important parameters that regulate the underlying mechanism of these LCOs while exhibiting a predator-prey like dynamic (note that other controlling parameters cannot be ruled out with the available data). To further explore this, we applied electron cyclotron heating (ECH) to an established wide-pedestal QH-mode discharge to vary both T_e and ∇T_e which surprisingly resulted in increase of thermal energy confinement time.

Figure 13 shows a wide-pedestal QH-mode discharge with ECH application at 4000 ms (~0.7 MW of ECH power is added at ρ~0.3 and an additional ~0.45 MW ECH power is added ~ 4300 ms). The NBI power remains constant (~4.1 MW) during ECH application as shown in figure 13a. After the ECH is applied, the energy confinement surprisingly increases as indicated by the increase in the value of ITER h98y2 scaling parameter in figure 13b. This is in contrast to confinement degradation[37, 38] with additional ECH power observed in normal H-mode plasmas with ELMs. Figure 13c shows ñ rms value obtained from DBS measurements at ρ~0.91. The LCOs can be seen clearly modulating measured density turbulence. The LCO frequency decreases (~63%) from ~77 Hz

Physics of Plasmas ACCEPTED MANUSCRIPT
This is the author's peer reviewed, accepted manuscript. However, the online version of record will be different from this version once it has been copyedited and typeset.
PLEASE CITE THIS ARTICLE AS DOI: 10.1063/1.5097143
AIP Publishing

before (~3800 ms) ECH application to ~28 Hz after ECH application (~4400 ms) but the peak turbulence amplitude has remained nearly the same i.e. less frequent ñ bursts with ECH. As expected this leads to a decrease in time-averaged ñ rms value at ρ~0.91 (shown in Figure 13d) which decreases from ~0.0028 before ECH application to ~0.0012 after ECH application i.e. ~57%. Figure 13e shows an increase in ∇T_e (~25%) measured at ρ~0.91 after ECH application and the LCO perturbations to ∇T_e also increase. Despite the increase in ∇T_e, density turbulence has decreased on average. This can be explained by increase (~50%) in $E \times B$ shear (figure 13f) at ρ~0.91 obtained from multi-radii DBS measurements of $v_{E\times B}$. The observed decrease in time-averaged ñ rms value with an increase in $v'_{E\times B}$ is consistent with confinement improvement (figure 13b) and also profile improvements observed in profiles of n_e and T_e shown in figure 14a-b for times before and after ECH application. Both pedestal pressure height and pedestal pressure gradient are found to increase after ECH application.

Additionally, ECH is found to be an actuator for LCO frequency control from the above observations. A survey of many discharges with different LCO frequencies has also shown (Figure 15) that both the LCO period and the perturbations from LCOs on ∇T_e increase with an increase in ∇T_e. This is consistent with observation in figure 13e. Future experiments and analysis will explore other possible actuators (e.g. $v'_{E\times B}$, collisionality, etc.) that can affect LCO dynamics and hence LCO period.

IX. Summary and future work

Long-lived limit cycle oscillation dynamics are observed in wide-pedestal QH-mode that is free of EHOs and ELMs. The appearance of these LCOs correlate with EHO cessation which depends on edge bootstrap current evolution after the wide-pedestal transition. The LCO dynamics have been explained on the basis of predator-prey behavior between different parameters like ∇T_e, ñ , and $v'_{E\times B}$. Unlike an ideal Lotka-Volterra predator-prey system, this observed system depends on the spatial and temporal variations e.g. in ∇T_e and $v_{E\times B}$. An inward radial propagation of the $v_{E\times B}$ perturbations generates the necessary velocity shear, $v'_{E\times B}$ which then regulates ñ locally. The underlying physical mechanism of the delay associated with the evolution of ñ and $v_{E\times B}$ at different radial locations is unknown so far. 1D modeling[39-41] of multifield predator-prey systems for LCOs during L-H transition might help us understand this delay mechanism. However, the long-lived LCOs described in this manuscript are found to have significant differences when compared to the transient LCOs observed preceding the L-H transition[12-15] bifurcation where turbulence feeds the zonal flow and in our case turbulence is observed to damp the mean $E \times B$ flow.

We also found other contrasting features of our long-lived LCOs which are very different from the transient LCOs observed during L-H transition such as our LCOs don't lead to any confinement transition whereas in the case of L-H transition , the LCO dynamics leads to the H-mode transition. The LCOs reported here are observed in an already developed pedestal whereas LCOs observed during L-H transition occur while the pedestal is dynamically evolving. These differences are summarized in Table 1.

Additionally, LCO dynamics have been modified by adding ECH. This led to improved particle and thermal confinement correlated with decreased time averaged ñ rms levels and higher $v'_{E\times B}$ indicating again the underlying turbulence associated with these LCOs contributes to the transport in the edge region of wide-pedestal QH-mode plasmas.

We have gained significant understanding of the LCOs in wide-pedestal QH-mode[42] and found that the underlying turbulence and transport have an important role in maintaining the wide-pedestal below the ELM-unstable limit. This is evident from the edge Langmuir probe ion saturation current density being modulated at the LCO frequency and also from the modifications of the LCO period with ECH leading to better particle and heat confinement. The dynamics and physics of an LCO/predator prey like regime in a developed and quasistationary wide-pedestal QH-mode was the focus of this paper. Future work will focus on the physics of the transition from standard to wide-pedestal QH-mode and the subsequent development of an LCO state.

Acknowledgement
This work was supported in part by the U.S. Department of Energy under Awards No. DE-FC02-04ER54698 and No. DE-FG02-08ER54984. This report was prepared as an account of work sponsored by an agency of the

ACCEPTED MANUSCRIPT
Physics of Plasmas
This is the author's peer reviewed, accepted manuscript. However, the online version of record will be different from this version once it has been copyedited and typeset.
PLEASE CITE THIS ARTICLE AS DOI: 10.1063/1.5097143
AIP Publishing

United States Government. Neither the United States Government nor any agency thereof, nor any of their employees, makes any warranty, express or implied, or assumes any legal liability or responsibility for the accuracy, completeness, or usefulness of any information, apparatus, product, or process disclosed, or represents that its use would not infringe privately owned rights. Reference herein to any specific commercial product, process, or service by trade name, trademark, manufacturer, or otherwise does not necessarily constitute or imply its endorsement, recommendation, or favoring by the United States Government or any agency thereof. The views and opinions of authors expressed herein do not necessarily state or reflect those of the United States Government or any agency thereof.

References

[1] F. Wagner, G. Fussmann, T. Grave, M. Keilhacker, M. Kornherr, K. Lackner, K. McCormick, E. R. Muller, A. Stabler, G. Becker *et al.*, Phys. Rev. Lett. 53, 1453 (1984).
[2] H. Zohm, Plasma Phys. Controlled Fusion 38, 105 (1996).
[3] A. Loarte, G. Saibene, R. Sartori, D. Campbell, M. Becoulet, L. Horton, T. Eich, A. Herrmann, G. Matthews, N. Asakura *et al*., Plasma Phys. Controlled Fusion 45, 1549 (2003).
[4] T. E. Evans, J. Nucl. Mater. 438, S11 (2013).
[5] ITER Physics Basis Editors, ITER Physics Expert Group Chairs and Co-Chairs, and ITER Joint Central Team and Physics Unit, Nucl. Fusion 39, 2137 (1999).
[6] K. H. Burrell, W. P. West, E. J. Doyle, M. E. Austin, T. A. Casper, P. Gohil, C. M. Greenfield, R. J. Groebner, A. W. Hyatt, R. J. Jayakumar *et al.,* Phys. Plasmas 12, 056121 (2005).
[7] W. Suttrop, V. Hynonen, T. Kurki-Suonio, P.T. Lang, M. Maraschek, R. Neu, A. Stabler, G.D. Conway, S. Hacquin, M. Kempenaars *et al.,* Nucl. Fusion 45, 721 (2005).
[8] Y. Sakamoto, H. Shirai, T. Fujita, S. Ide, T. Takizuka, N. Oyama, and Y. Kamada, Plasma Phys. Controlled Fusion 46, A299 (2004).
[9] B. A. Grierson, K. H. Burrell , R. M. Nazikian, W. M. Solomon, A. M. Garofalo, E. A. Belli , G. M. Staebler , M. E. Fenstermacher, G. R. McKee, T. E. Evans *et al.,* Phys. Plasmas 22, 055901 (2015).
[10] K. H. Burrell , K. Barada , X. Chen, A. M. Garofalo, R. J. Groebner, C. M. Muscatello , T. H. Osborne, C. C. Petty, T. L. Rhodes, P. B. Snyder *et al.,* Phys. Plasmas 23, 056103 (2016).
[11] Xi Chen, K.H. Burrell, T.H. Osborne, W.M. Solomon, K. Barada, A.M. Garofalo, R.J. Groebner, N.C. Luhmann, G.R. McKee, C.M. Muscatello *et al.,* Nucl. Fusion 57, 022007 (2017).
[12] L. Schmitz, L. Zeng, T. L. Rhodes, J. C. Hillesheim, E. J. Doyle, R. J. Groebner, W. A. Peebles, K. H. Burrell, and G. Wang, Phys. Rev. Lett. 108, 155002 (2012).
[13] J. Cheng, J.Q. Dong, K. Itoh, L.W. Yan, W.Y. Hong, K.J. Zhao, Z.H. Huang, X.Q. Ji, W.L. Zhong, D.L. Yu *et al.,* Nucl. Fusion Phys. 54, 114004 (2014).
[14] T. Estrada, T. Happel, C. Hidalgo, E. Ascasíbar, and E.Blanco, Europhys. Lett. 92, 35001 (2010).
[15] G. S. Xu, B. N. Wan, H. Q. Wang, H. Y. Guo, H. L. Zhao, A. D. Liu, V. Naulin, P. H. Diamond, G. R. Tynan, M. Xu *et al.,* Phys. Rev. Lett. 107, 125001 (2011).
[16] J. L. Luxon, Nucl. Fusion 42, 614 (2002).
[17] W. A. Peebles, T. L. Rhodes, J. C. Hillesheim, L. Zeng, and C. Wannberg, Rev. Sci. Instrum. 81, 10D902 (2010).
[18] M Hirsch and E Holzhauer, Plasma Phys. Control. Fusion 46, 593 (2004)
[19] P. Hennequin, C. Honoré, A. Truc, A. Quéméneur, N. Lemoine, J.-M. Chareau, and R. Sabot, Rev. Sci. Instrum. 75, 3881 (2004)
[20] J.C. Hillesheim, N.A. Crocker, W.A. Peebles, H. Meyer, A. Meakins, A.R. Field, D. Dunai, M. Carr, N. Hawkes, Nucl. Fusion 55, 073024 (2015).
[21] P Hennequin, C Honoré, A Truc, A Quéméneur, C Fenzi-Bonizec, C Bourdelle, X Garbet, G.T Hoang, and the Tore Supra team, Nucl. Fusion 46, S771 (2006).
[22] G D Conway, J Schirmer, S Klenge, W Suttrop, E Holzhauer, and the ASDEX Upgrade Team, Plasma Phys. Controlled Fusion 46, 951 (2004).

ACCEPTED MANUSCRIPT
Physics of Plasmas
This is the author's peer reviewed, accepted manuscript. However, the online version of record will be different from this version once it has been copyedited and typeset.
PLEASE CITE THIS ARTICLE AS DOI: 10.1063/1.5097143
AIP Publishing

[23] J. C. Hillesheim, W. A. Peebles, T. L. Rhodes, L. Schmitz, T. A. Carter, P.-A. Gourdain, and G. Wang, Rev. Sci. Instrum. 80, 083507 (2009).
[24] J. Q. Hu, C. Zhou, A. D. Liu, M. Y. Wang, E. J. Doyle, W. A. Peebles, G. Wang, X. H. Zhang, J. Zhang, X. Feng *et al*, Rev. Sci. Instrum. 88, 073504 (2017)
[25] A. P. Smirnov, R. W. Harvey, and R. Prater, in Proceedings of the 15th Workshop on ECE and ECRH (World Scientific, Singapore, 2009), p. 301; also see www.compxco.com/genray.html.
[26] G. M. Staebler, J. E. Kinsey, and R. E. Waltz, Phys. Plasmas14, 055909 (2007).
[27]L. Zeng, K. Barada, W. Peebles, and T. Rhodes, Bulletin of the American Physical Society (2018).
[28] P.B. Snyder, K.H. Burrell, H.R. Wilson, M.S. Chu, M.E. Fenstermacher, A.W. Leonard, R.A. Moyer, T.H. Osborne, M. Umansky, W.P. West, and X.Q. Xu, Nucl. Fusion 47, 961 (2007).
[29] A. Diallo, R. J. Groebner, T. L. Rhodes, D. J. Battaglia, D. R. Smith, T. H. Osborne, J. M. Canik, W. Guttenfelder, and P. B. Snyder, Phys. Plasmas 22, 056111 (2015).
[30] P. H. Diamond, S-I Itoh, K. Itoh, and T. S. Hahm, Plasma Phys. Control. Fusion 47, R35 (2005)
[31] H. Biglari, P. H. Diamond, and P. W. Terry, Phys. Fluids B **2** 1 (1990)
[32] C. Elton and M. Nicholson, Journal of Animal Ecology 11, 215 (1942).
[33] W. G. Wilson, A. M. de Roos, and E. McCauley, Theor. Popul. Biol. 43, 91 (1993).
[34] B. Kerr, C. Neuhauser, B. J. Bohannan, and A. M. Dean, Nature 442, 75 (2006).
[35] R. Abta, M. Schiffer, and N. M. Shnerb, Phys. Rev. Lett. 98,098104 (2007).
[36]J. Wesson and D. J. Campbell. Tokamaks. Vol. 149. Oxford University Press, 2011.
[37] X. Wang, S. Mordijck, E.J. Doyle, T.L. Rhodes, L. Zeng, G.R. McKee, M.E. Austin, O. Meneghini, G.M. Staebler and S.P. Smith, Nucl. Fusion 57**,** 116046 (2017).
[38] S. Mordijck, X. Wang, E.J. Doyle, T.L. Rhodes, L. Schmitz, L. Zeng, G.M. Staebler, C.C. Petty, R.J. Groebner, W.-H. Ko *et al*, Nucl. Fusion 55, 113025 (2015).
[39] K. Miki, P. H. Diamond, Ö. D. Gürcan, G. R. Tynan, T. Estrada, L. Schmitz, and G. S. Xu, Phys. Plasmas 19, 092306 (2012).
[40] B. A. Carreras, D. Newman, P. H. Diamond, and Y.-M. Liang **,** Physics of Plasmas 1, 4014 (1994).
[41] M. A. Malkov , P. H. Diamond, K. Miki, J. E. Rice, and G. R. Tynan, Phys. Plasmas 22, 032506 (2015).
[42]K. Barada, T. L. Rhodes, K. H. Burrell, L. Zeng, L. Bardoczi, Xi Chen, C. M. Muscatello, and W. A. Peebles, Phys. Rev. Lett 120, 135002, (2018).

FIGURE CAPTIONS

Physics of Plasmas ACCEPTED MANUSCRIPT
This is the author's peer reviewed, accepted manuscript. However, the online version of record will be different from this version once it has been copyedited and typeset.
PLEASE CITE THIS ARTICLE AS DOI: 10.1063/1.5097143
AIP Publishing

Figure 1. Temporal variations of (a) NBI power, (b)NBI torque, (c) EHO amplitude, (d) Chord averaged density (e) Electron pedestal pressure, and (f) Electron pedestal width for a high (black) and a low (red) target density QH-mode discharges with their respective wide-pedestal transition times marked by black and red dash-dot vertical lines.

Figure 2. (a) Electron pedestal pressure, (b) its gradient and (c) calculated edge bootstrap current before (black solid curve) and after (blue dot-dash curve) wide-pedestal transition in high target density shot where the EHO reappears after the transition and (d) Electron pedestal pressure, (e) its gradient and (f) calculated edge bootstrap current before (black solid curve) and after (blue dot-dash curve) wide-pedestal transition in low target density shot where the EHO turns off and does not reappear after the transition.

Figure 3. (a) T_e at ρ ~ 0.91 and C^{6+} T_i at ρ ~ 0.90 , (b) Lower divertor Dα visible light emission intensity, (c) Ion saturation current density from edge Langmuir probe, and (d) Radial electric field measured by CER

Figure 4. (a) Black and red arrows shown on the temporal variations of T_e at ρ ~ 0.91 correspond to the beginning and end of a limit cycle, the times for which the radial profiles of (b) electron density, (c) electron temperature, and (d) electron pressure are shown with respective colors (i.e. black and red solid curves correspond to the profiles at times around the beginning and end of an LCO cycle). Horizontal and vertical dash-dot lines in red and black are indicative of respective changes in electron pressure pedestal height and width during an LCO cycle.

Figure 5. (a) Density pedestal height, (b) density pedestal width estimated from tanh fitting of high time resolution profile reflectometry density measurements show larger relative increase in density pedestal width compared to the height which leads to decrease in pedestal density gradient (c) which is calculated from data in (a) and (b), and (d) edge Te variations during limit cycle oscillations in a wide-pedestal QH-mode discharge.

Figure 6. Pedestal gradients of electron density measured by profile reflectometry at (a) ρ~0.94 and (b) ρ~0.88, Pedestal gradients of electron temperature measured by electron cyclotron emission diagnostics at (c) ρ~0.94 and (d) ρ~0.88, and Pedestal gradients of electron pressure obtained from (a), (b), (c), and (d) by multiplying the electron density and temperature gradients at (e) ρ~0.94 and (f) ρ~0.88. All the gradients oscillate at the LCO frequency. Variations at ρ~0.88 follow the variations at ρ~0.94.

Figure 7. (a) DBS measured density fluctuation intensity spectrum showing regular bursts in the LCO regime, (b) ñ rms, (c) $v_{E\times B}$, (d) Electron temperature gradient, and (e) ExB shear all at ρ~0.91 during 50 ms of an LCO dominated phase in wide-pedestal QH-mode.

Figure 8. (a) Phase space $v_{E\times B}$ and ñ, (b) Phase space $v'_{E\times B}$ and ñ , and (c) Phase space of ∇T_e and ñ all at ρ~0.91 showing LCO behavior.

Figure 9. Temporal variations of (a) ñ rms values and (b) ExB velocity at three different pedestal locations (ρ~0.92, 0.90, and 0.88) during the LCO phase for ~ 3 LCO periods, and (c) temporal variations of ExB shear calculated at ρ~0.90.

Figure 10. A schematic cartoon showing the predator-prey dynamics as understood from our experimental results. The dynamics leading to LCOs during L-H transition are shown with dashed rectangular boxes and arrows on top left of this figure.

Figure 11. Individual contributions to the total radial electric field from diamagnetic pressure gradient and $V \times B$ forces measured by CER diagnostics of C^{6+}ions at three different major radius locations (a) Rmaj~223.5 cm, (b) Rmaj~225.0 cm, and (c) Rmaj~226.5 cm. Legends are shown in (c).

Figure 12. Comparisons of cross-correlation coefficients of $v_{E\times B}$ oscillations measured by two independent DBS systems toroidal and poloidally separated by 180º and ~9 cm before (solid black curve) and in (solid red curve) the LCO regime.

Figure 13. (a) Temporal variations of ECH and NBI power, (b) ITER h98y2 factor showing confinement improvement with ECH, (c) DBS measured ñ rms values around ρ~0.91 are modulated by the LCOs show a decrease in LCO modulation frequency, (d) Time averaged ñ shows a decrease in ñ with ECH, (e) edge ∇T_e (ρ~0.91) shows an increase with ECH and an increased LCO

ACCEPTED MANUSCRIPT
Physics of Plasmas
This is the author's peer reviewed, accepted manuscript. However, the online version of record will be different from this version once it has been copyedited and typeset.
PLEASE CITE THIS ARTICLE AS DOI: 10.1063/1.5097143
AIP Publishing

perturbations to ∇T_e with ECH, and (f) $E \times B$ shear (around ρ~0.91) calculated from DBS measurements of $E \times B$ velocity shows an increase with ECH in a beam heated discharge which is already in wide-pedestal QH-mode discharge prior to ECH application.

Figure 14. Comparisons of radial electron density and temperature profiles for no added ECH (black curve) and 1.2 MW ECH (red curve) added conditions in an already existing wide-pedestal QH-mode discharge show improvements in both particle and heat confinement.

Figure 15. ∇T_e vs LCO period from ~20 shots at multiple times. ∇T_e and the LCO perturbations to ∇T_e increase for increased LCO period.

TABLES

Wide-pedestal QH-mode LCOs	**LCOs during L-H transition**
Long-lived with no transition	Transient and Leads to L-H transition
ñ driven transport decreases gradients and ExB velocity	ñ driven zonal flow shear helps reduces transport i.e. increases gradients
ExB Flow shear regulates turbulence	Zonal flow shear regulates turbulence
LCOs are observed in an already developed pedestal	Pedestal dynamically develops during the course of LCOs

Table 1. Characteristics comparisons between LCOs observed in wide-pedestal QH-mode and LCOs observed during L-H transition.

ACCEPTED MANUSCRIPT
Physics of Plasmas
This is the author's peer reviewed, accepted manuscript. However, the online version of record will be different from this version once it has been copyedited and typeset.
PLEASE CITE THIS ARTICLE AS DOI: 10.1063/1.5097143
AIP Publishing

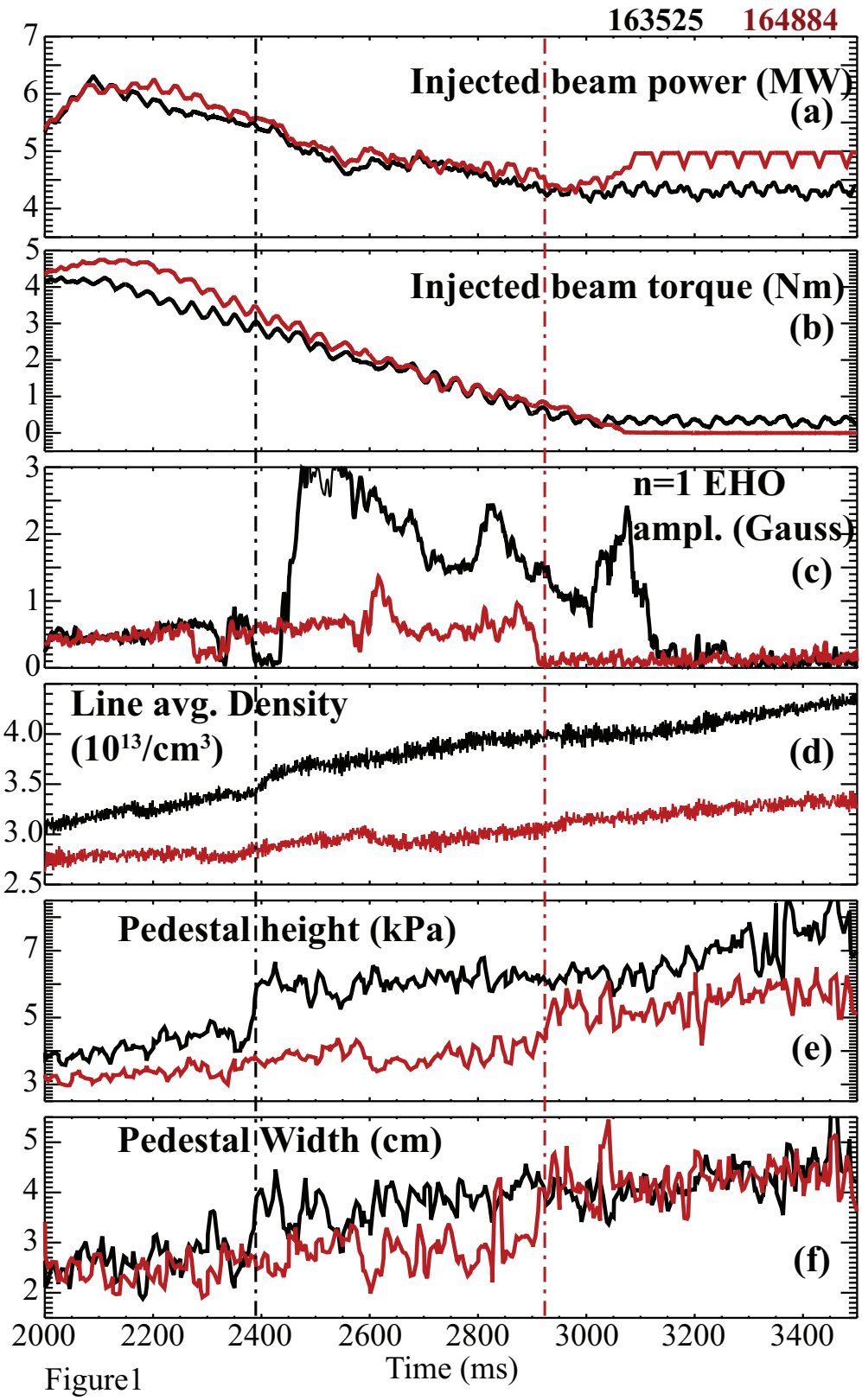

Figure1

ACCEPTED MANUSCRIPT
Physics of Plasmas
This is the author's peer reviewed, accepted manuscript. However, the online version of record will be different from this version once it has been copyedited and typeset.
PLEASE CITE THIS ARTICLE AS DOI: 10.1063/1.5097143
AIP Publishing

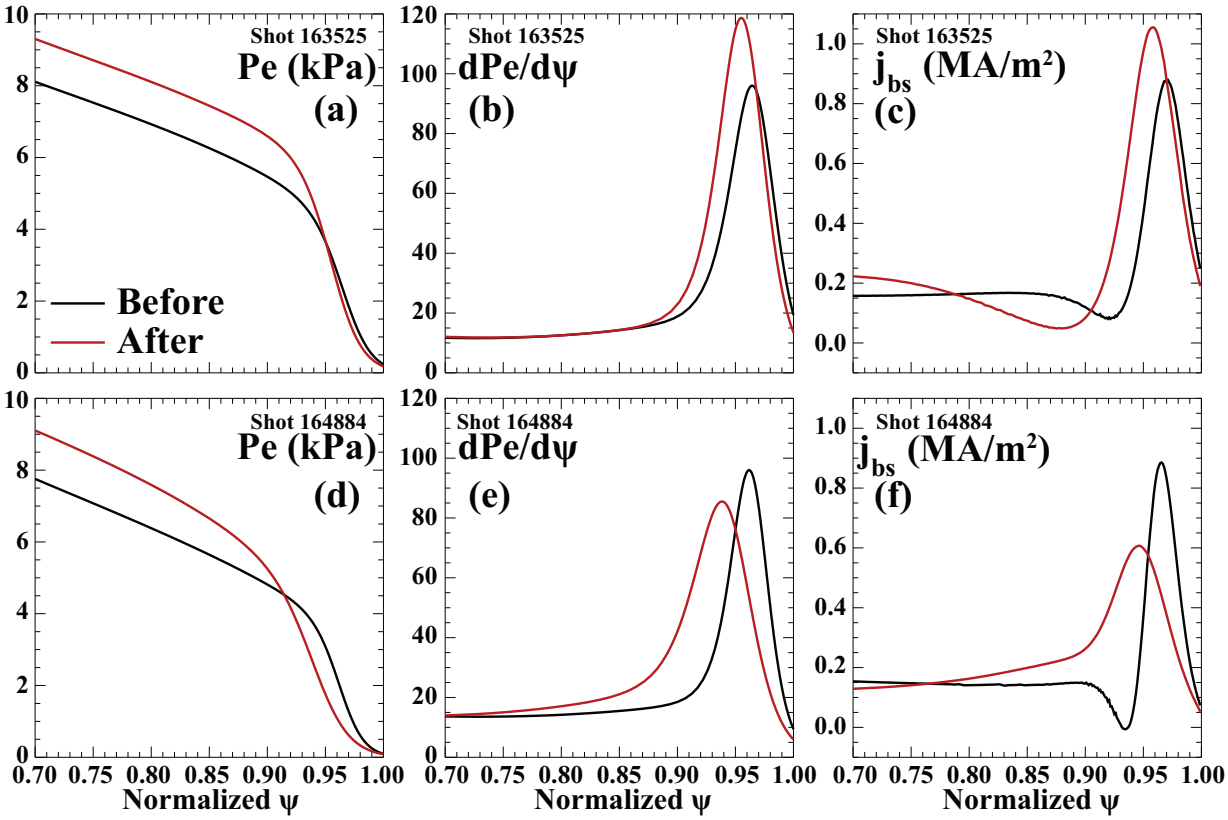

Figure 2

ACCEPTED MANUSCRIPT
Physics of Plasmas
This is the author's peer reviewed, accepted manuscript. However, the online version of record will be different from this version once it has been copyedited and typeset.
PLEASE CITE THIS ARTICLE AS DOI: 10.1063/1.5097143
AIP Publishing

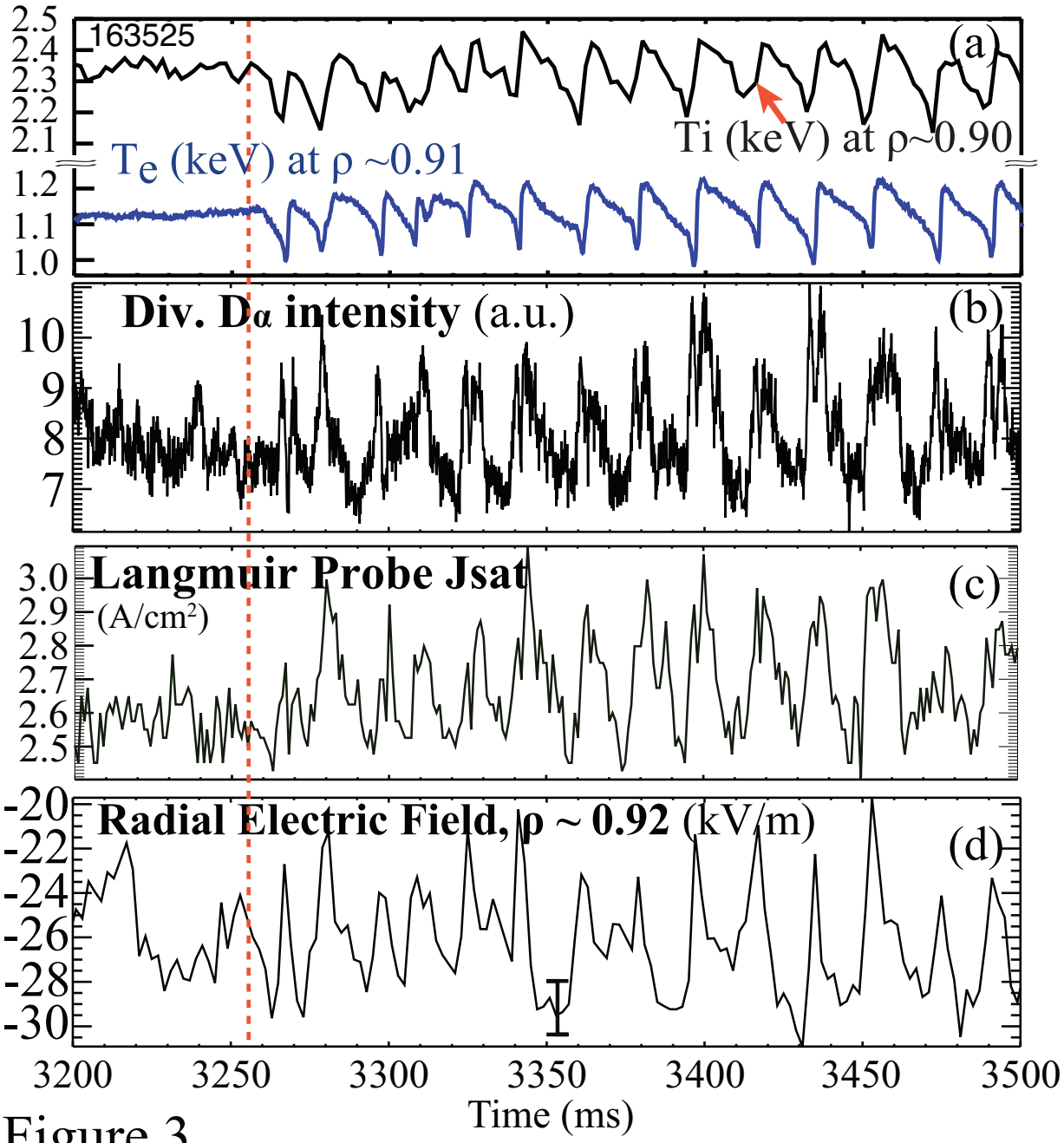

Figure 3

ACCEPTED MANUSCRIPT
Physics of Plasmas
This is the author's peer reviewed, accepted manuscript. However, the online version of record will be different from this version once it has been copyedited and typeset.
PLEASE CITE THIS ARTICLE AS DOI: 10.1063/1.5097143
AIP Publishing

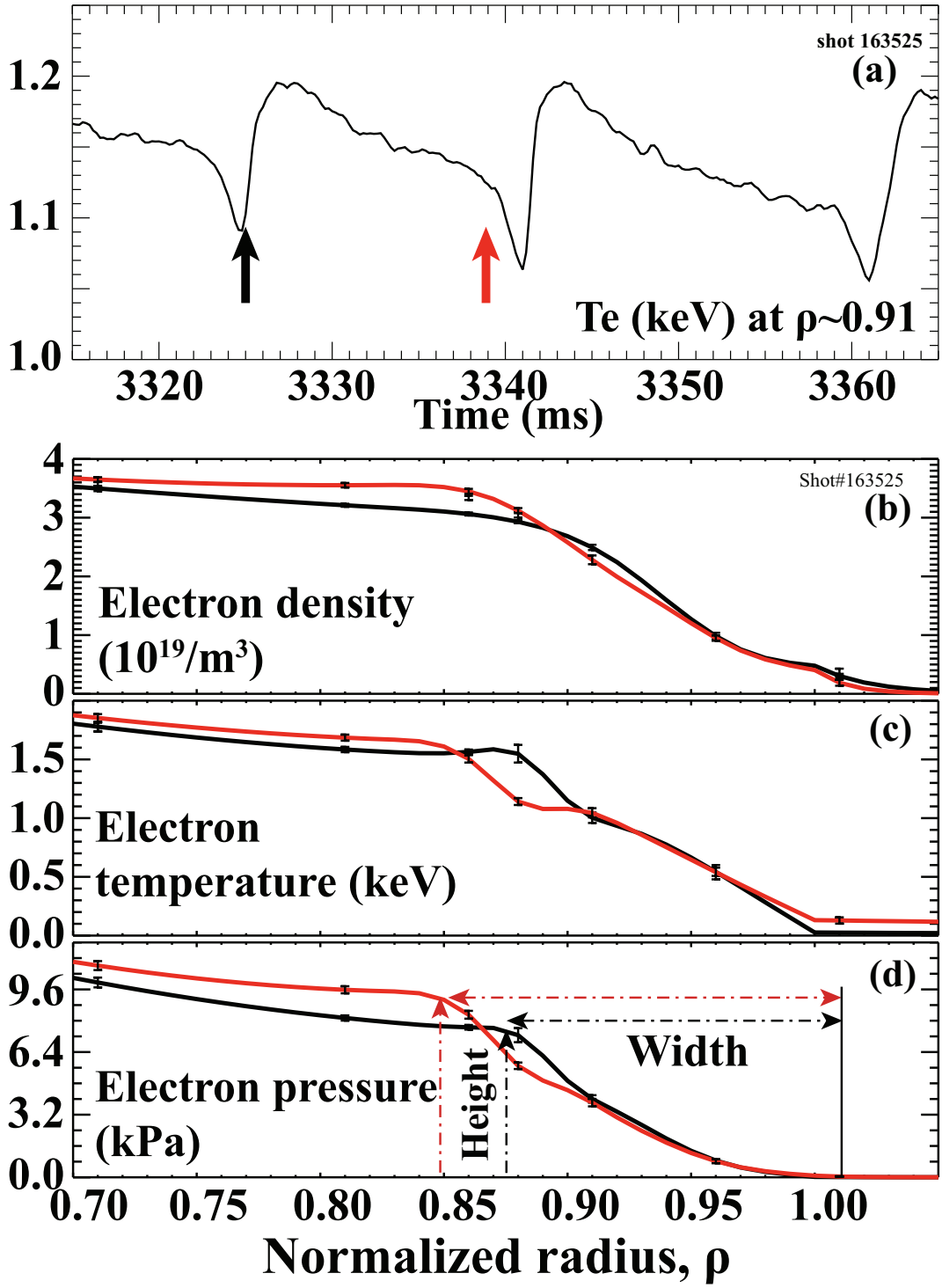

Figure 4

ACCEPTED MANUSCRIPT
Physics of Plasmas
This is the author's peer reviewed, accepted manuscript. However, the online version of record will be different from this version once it has been copyedited and typeset.
PLEASE CITE THIS ARTICLE AS DOI: 10.1063/1.5097143
AIP Publishing

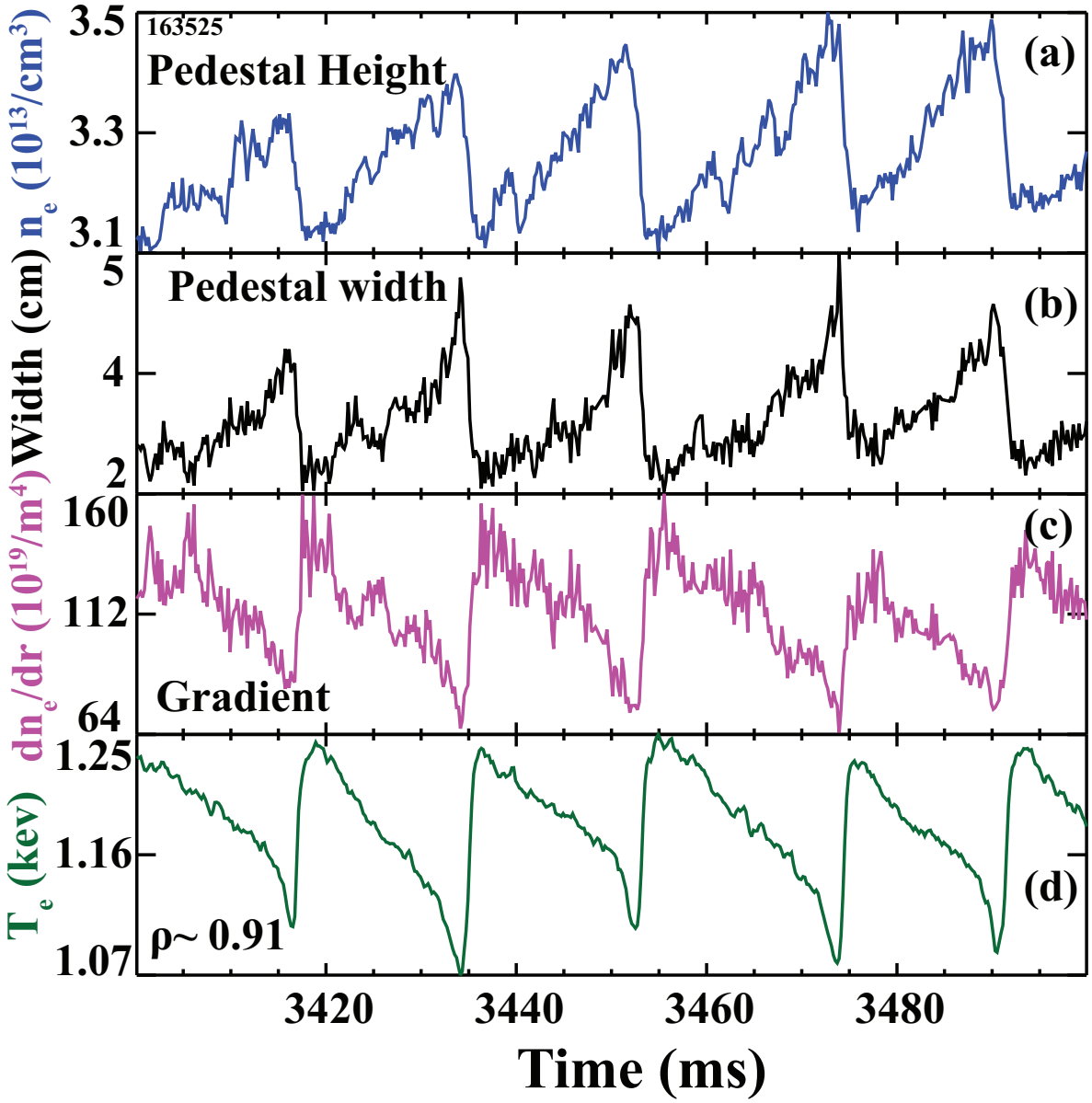

Figure 5

ACCEPTED MANUSCRIPT
Physics of Plasmas
This is the author's peer reviewed, accepted manuscript. However, the online version of record will be different from this version once it has been copyedited and typeset.
PLEASE CITE THIS ARTICLE AS DOI: 10.1063/1.5097143
AIP Publishing

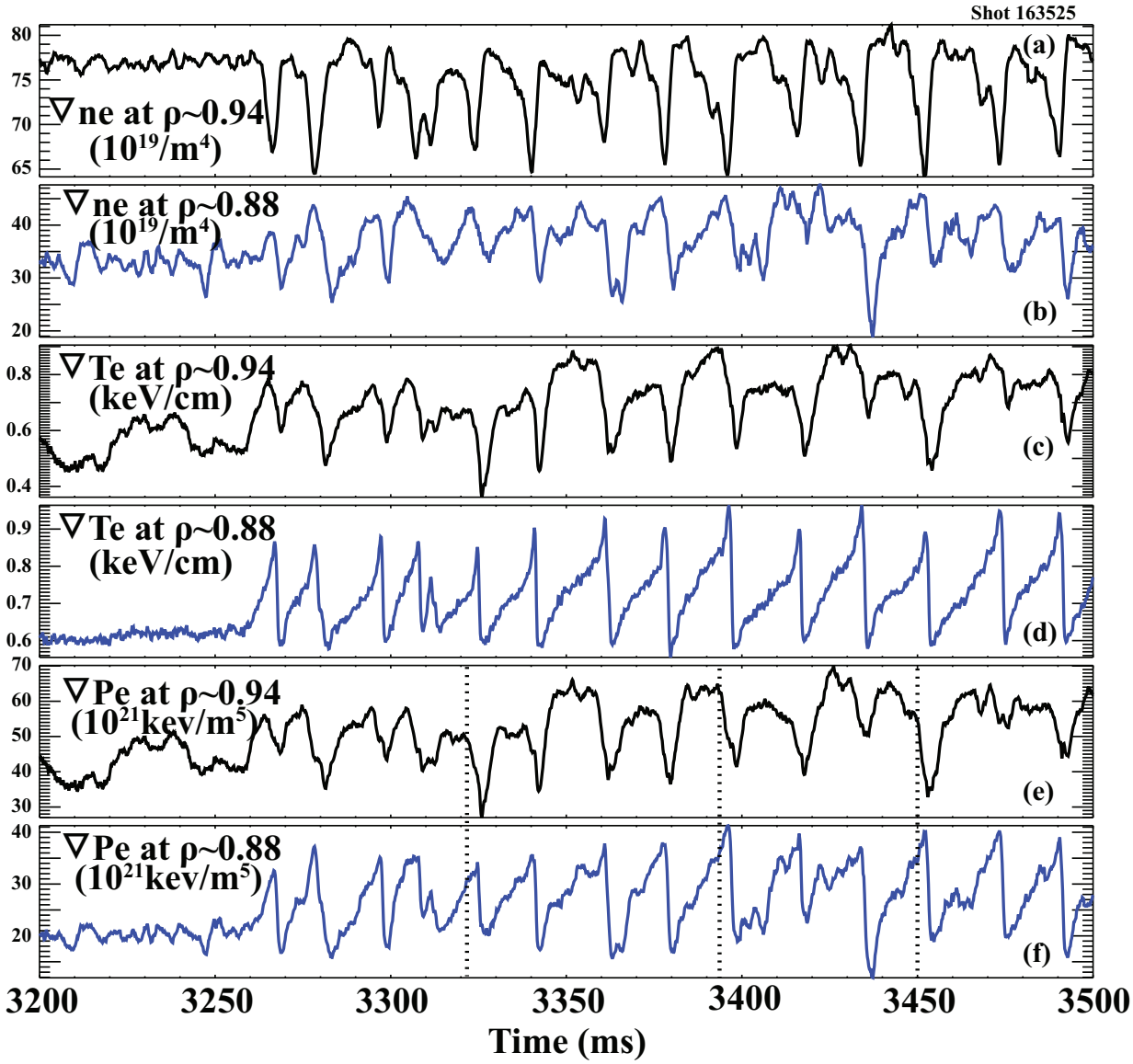

Figure 6

ACCEPTED MANUSCRIPT
Physics of Plasmas
This is the author's peer reviewed, accepted manuscript. However, the online version of record will be different from this version once it has been copyedited and typeset.
PLEASE CITE THIS ARTICLE AS DOI: 10.1063/1.5097143
AIP Publishing

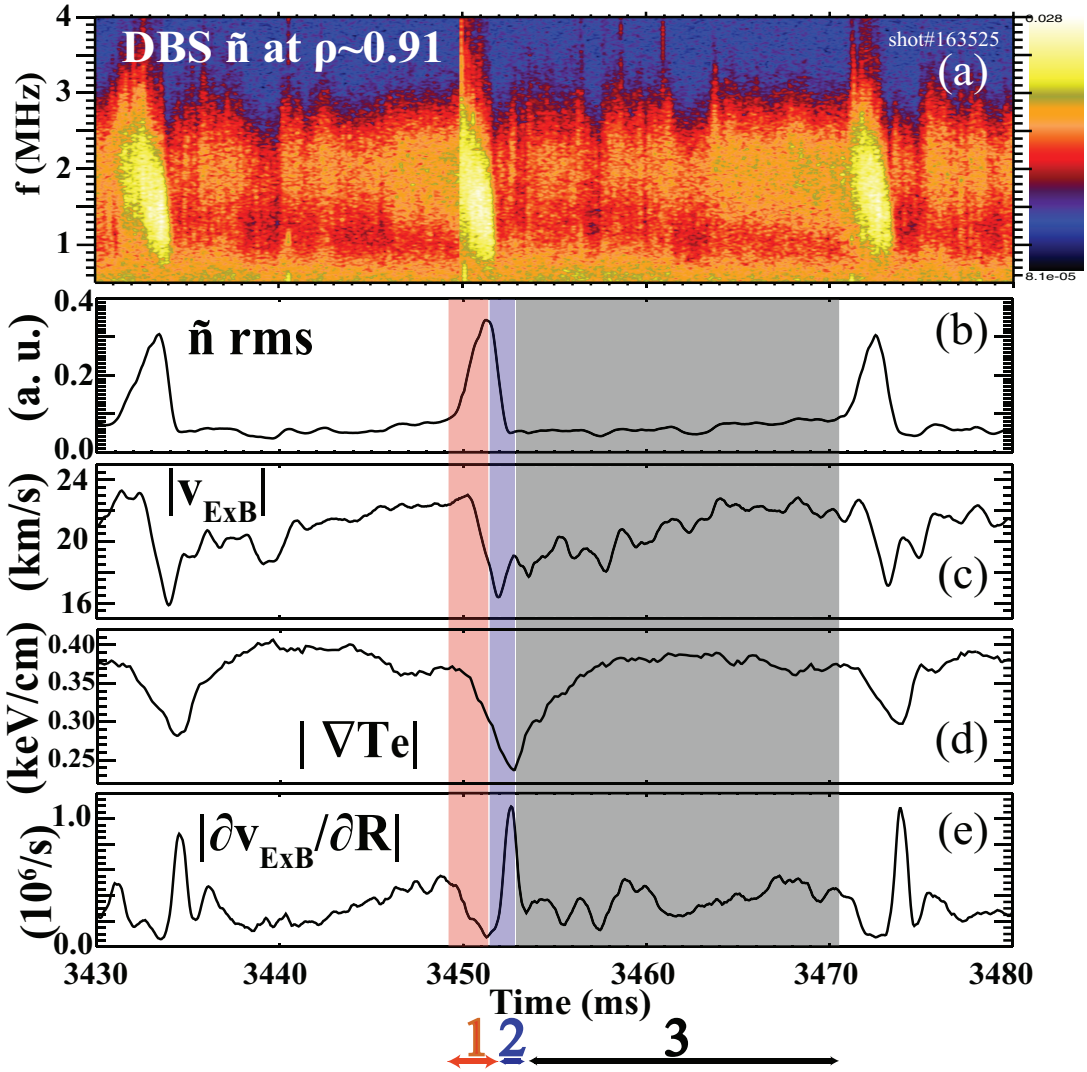

Figure 7

ACCEPTED MANUSCRIPT
Physics of Plasmas
This is the author's peer reviewed, accepted manuscript. However, the online version of record will be different from this version once it has been copyedited and typeset.
PLEASE CITE THIS ARTICLE AS DOI: 10.1063/1.5097143
AIP Publishing

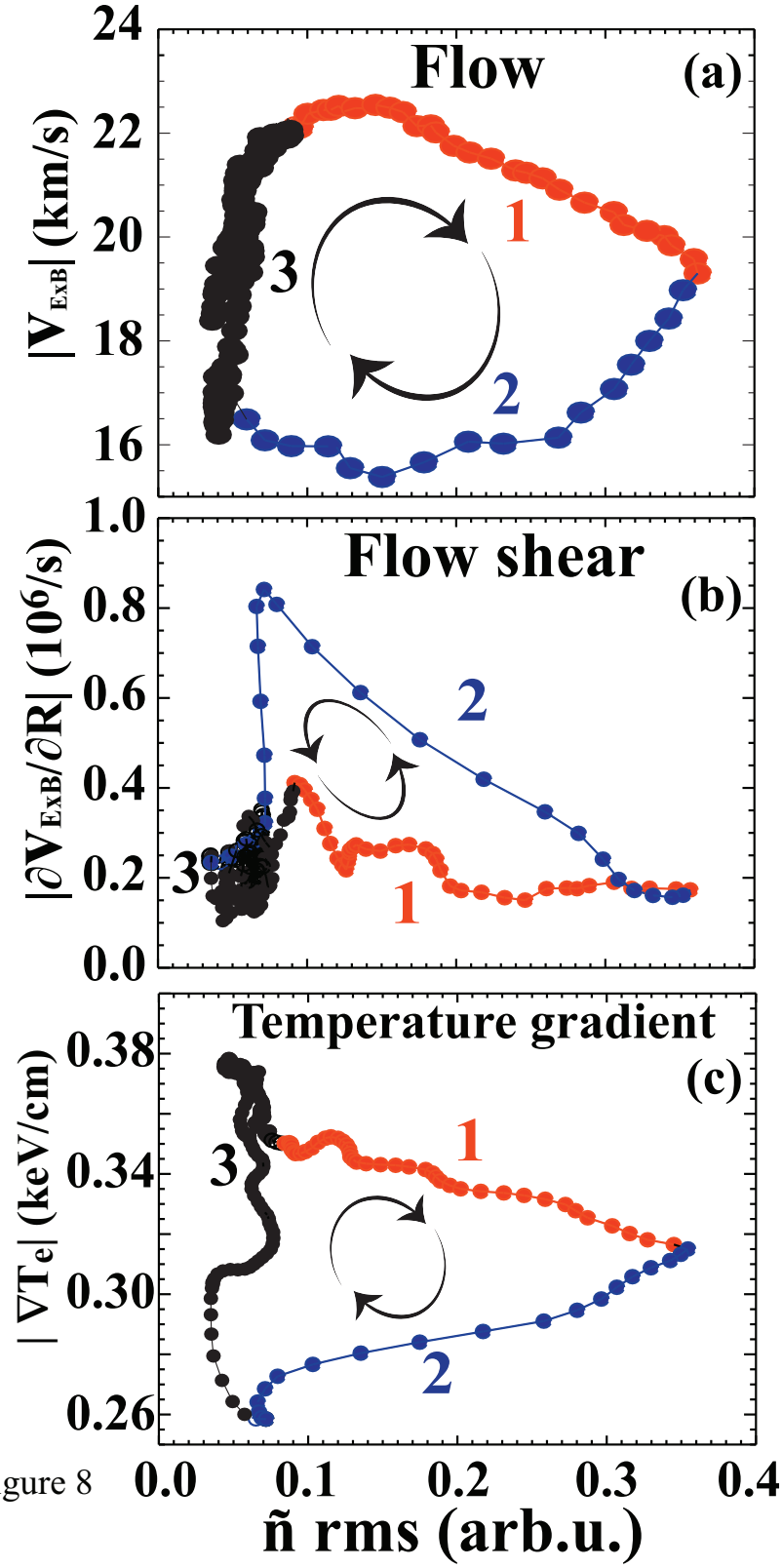

Figure 8

ACCEPTED MANUSCRIPT
Physics of Plasmas
This is the author's peer reviewed, accepted manuscript. However, the online version of record will be different from this version once it has been copyedited and typeset.
PLEASE CITE THIS ARTICLE AS DOI: 10.1063/1.5097143
AIP Publishing

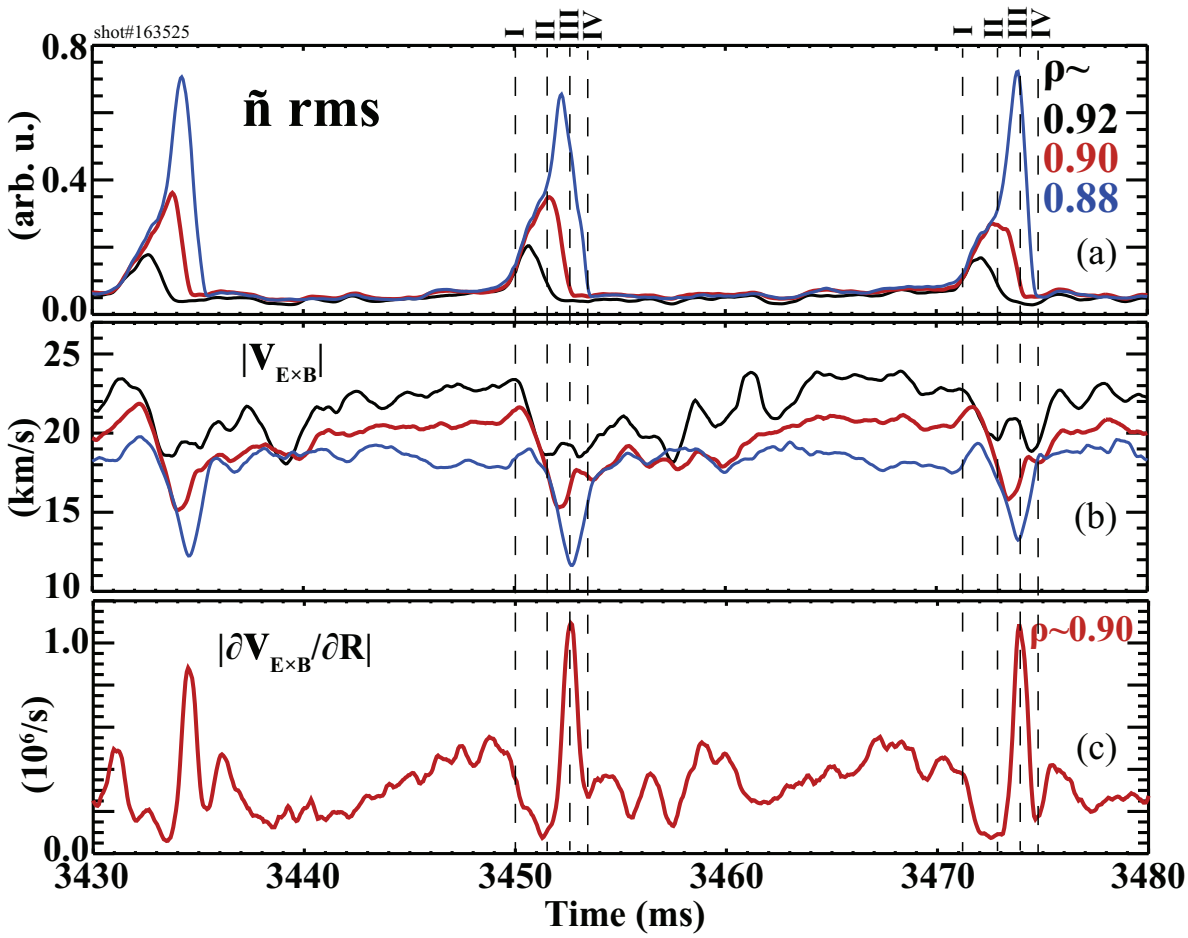

Figure 9

AIP Publishing
Physics of Plasmas
ACCEPTED MANUSCRIPT
This is the author's peer reviewed, accepted manuscript. However, the online version of record will be different from this version once it has been copyedited and typeset.
PLEASE CITE THIS ARTICLE AS DOI: 10.1063/1.5097143

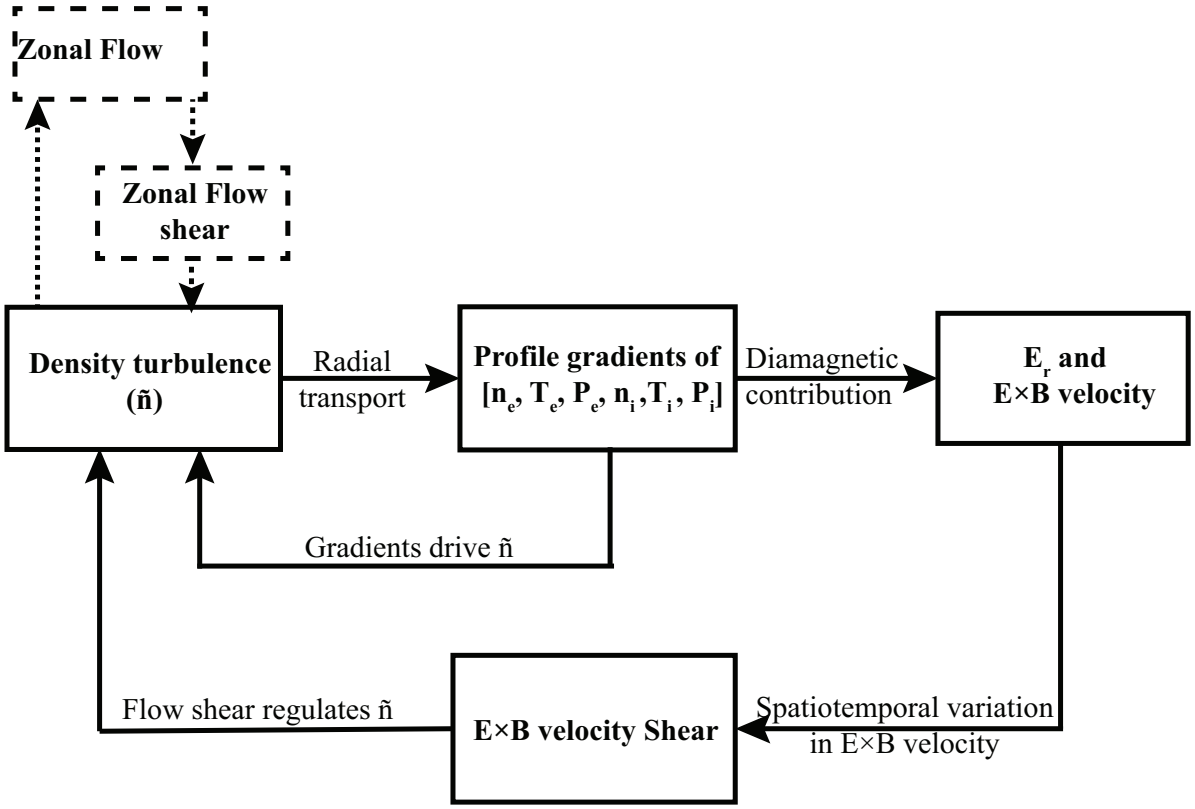

Figure 10

ACCEPTED MANUSCRIPT
Physics of Plasmas
This is the author's peer reviewed, accepted manuscript. However, the online version of record will be different from this version once it has been copyedited and typeset.
PLEASE CITE THIS ARTICLE AS DOI: 10.1063/1.5097143
AIP Publishing

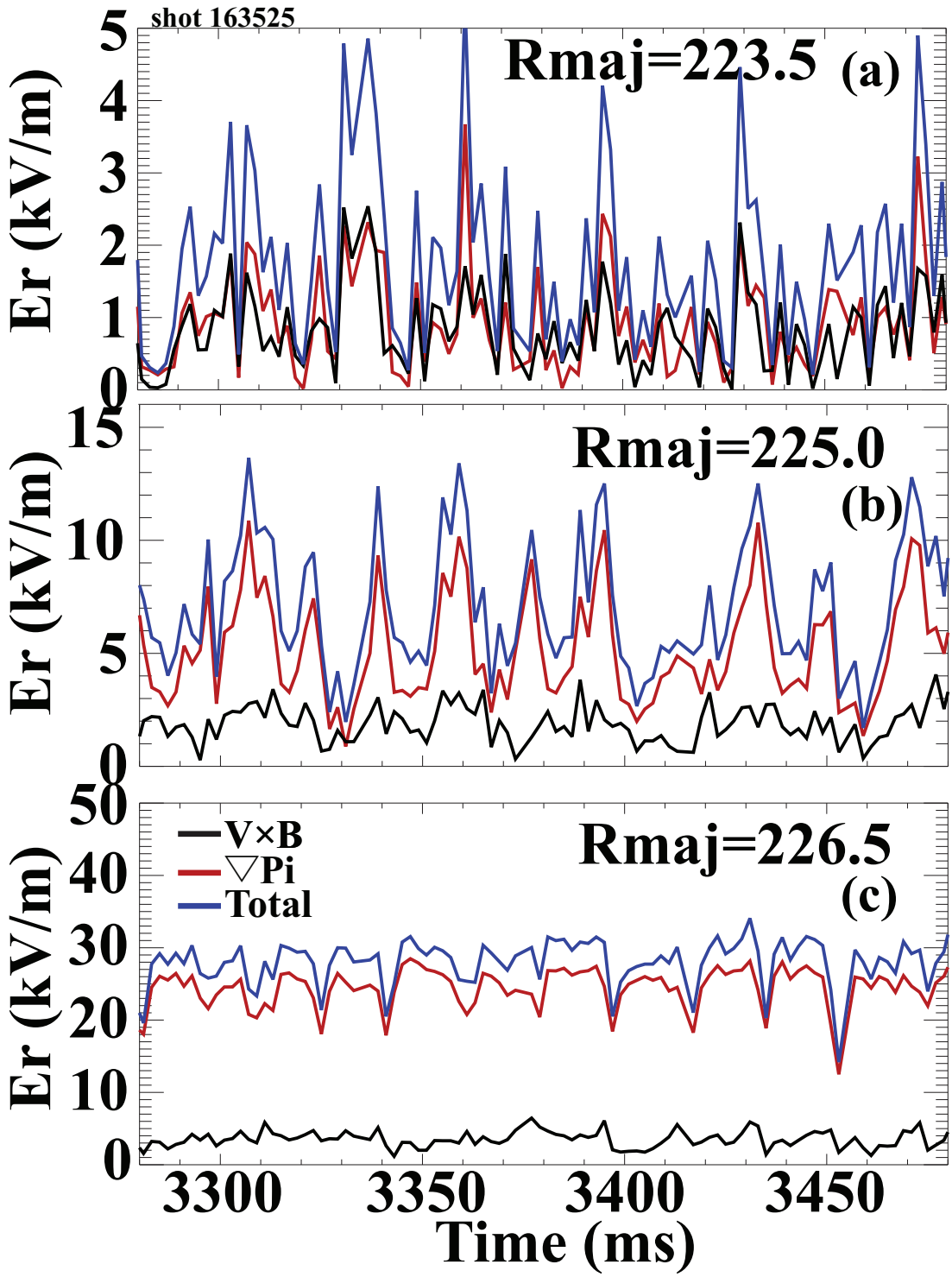

Figure 11

ACCEPTED MANUSCRIPT
Physics of Plasmas
This is the author's peer reviewed, accepted manuscript. However, the online version of record will be different from this version once it has been copyedited and typeset.
PLEASE CITE THIS ARTICLE AS DOI: 10.1063/1.5097143
AIP Publishing

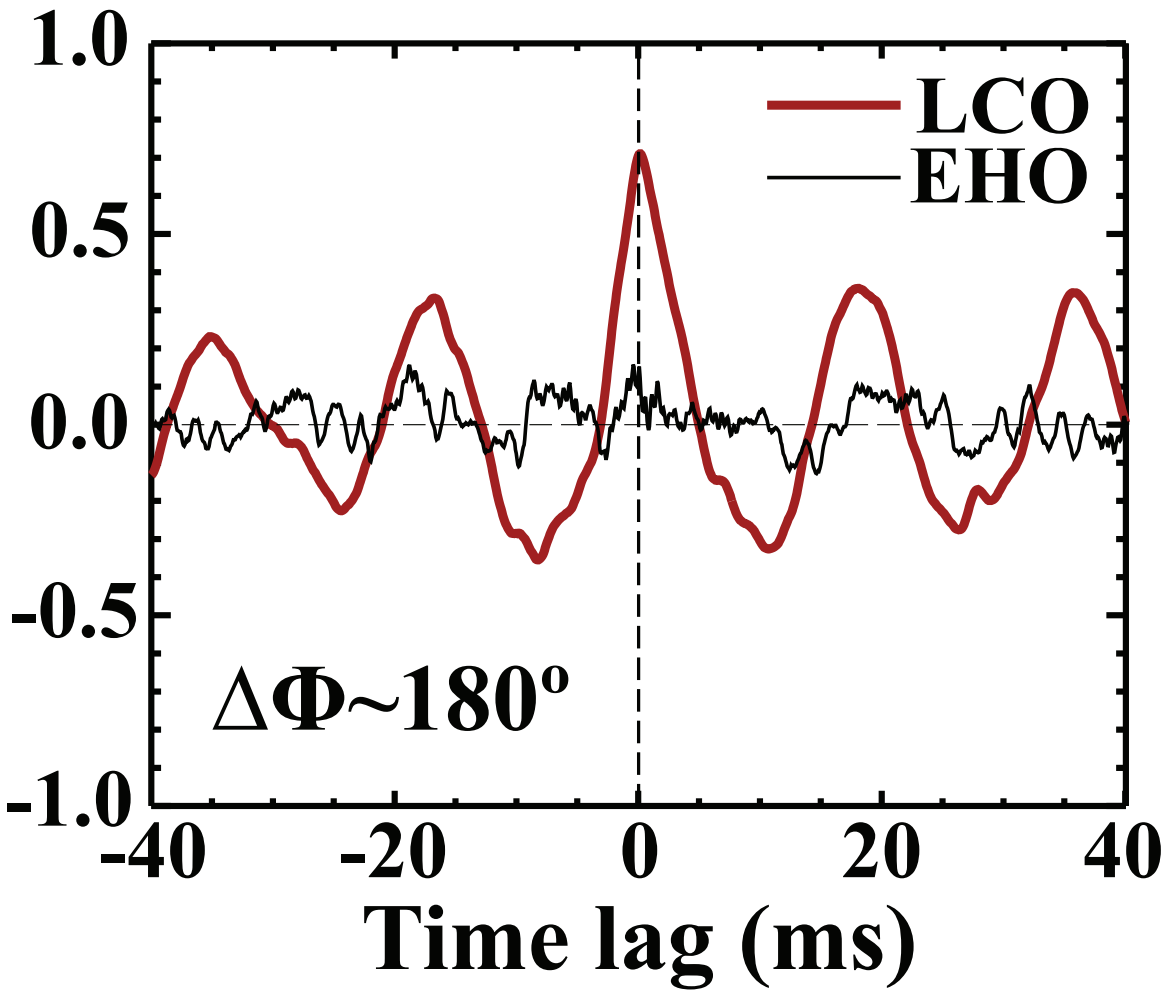

Figure 12

ACCEPTED MANUSCRIPT
Physics of Plasmas
This is the author's peer reviewed, accepted manuscript. However, the online version of record will be different from this version once it has been copyedited and typeset.
PLEASE CITE THIS ARTICLE AS DOI: 10.1063/1.5097143
AIP Publishing

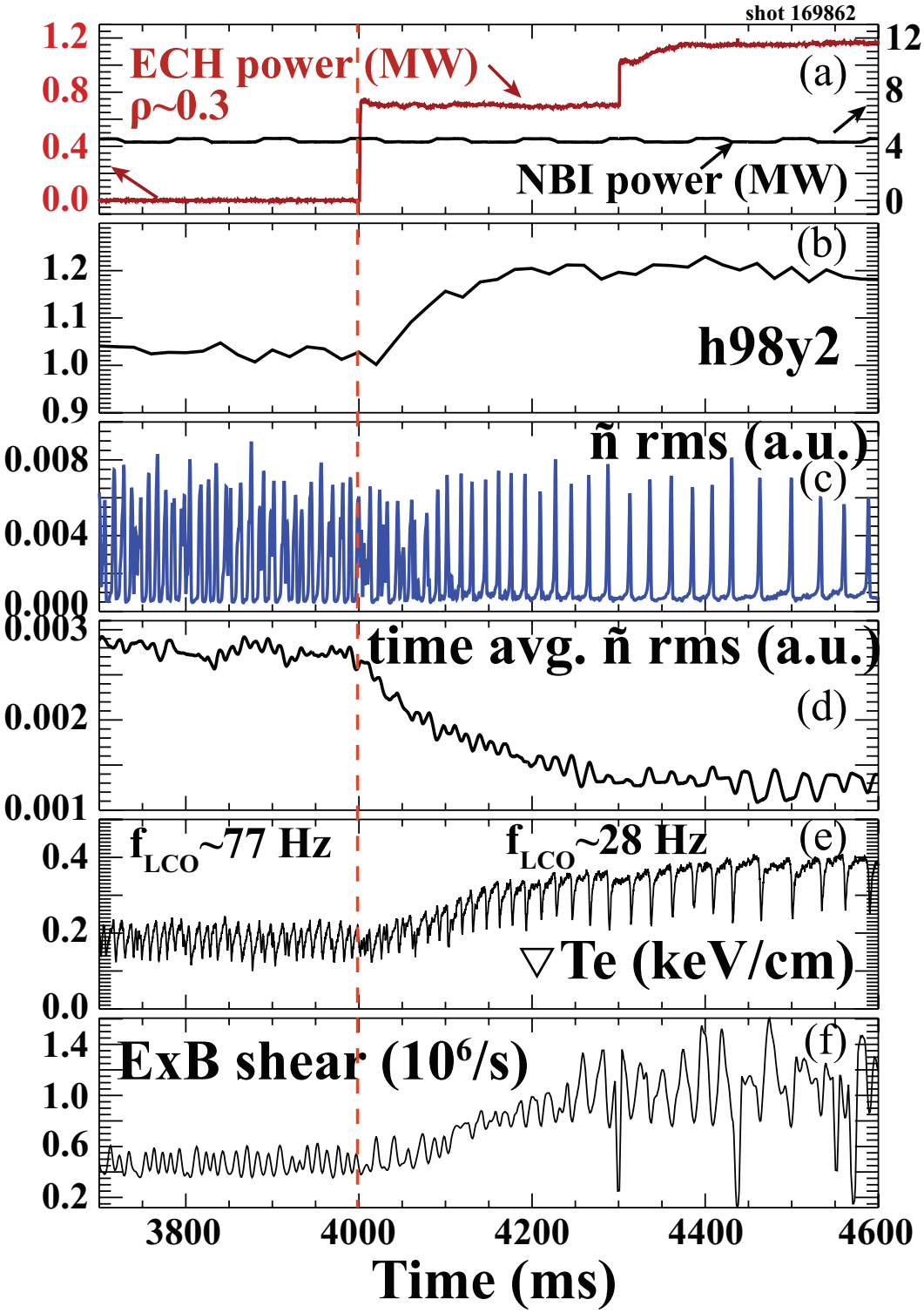

Figure 13

ACCEPTED MANUSCRIPT
Physics of Plasmas
This is the author's peer reviewed, accepted manuscript. However, the online version of record will be different from this version once it has been copyedited and typeset.
PLEASE CITE THIS ARTICLE AS DOI: 10.1063/1.5097143
AIP Publishing

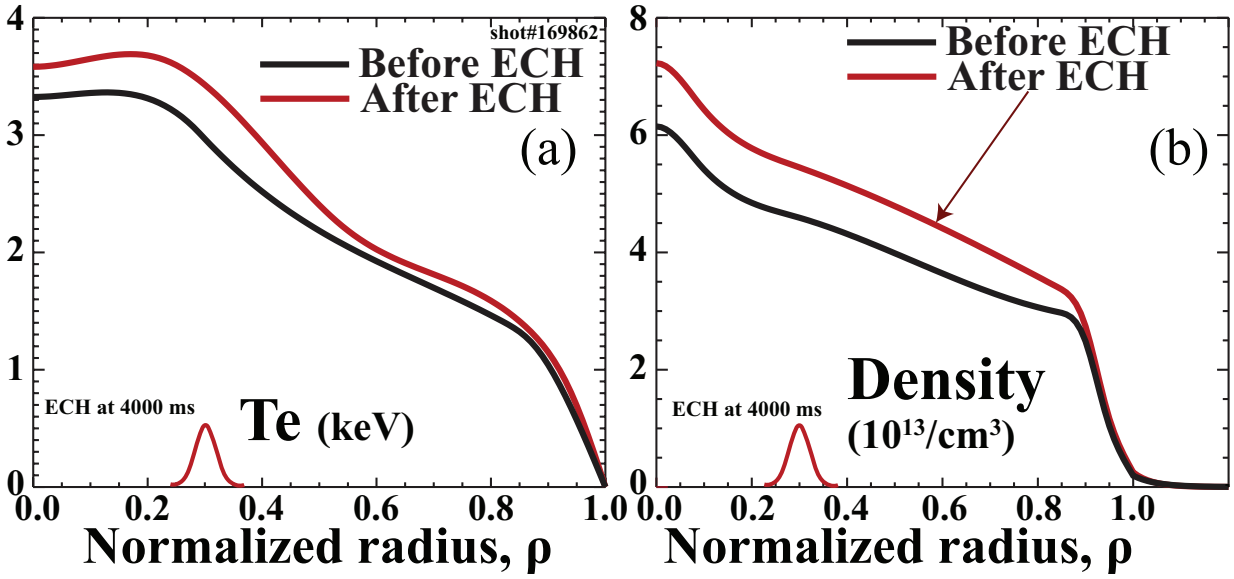

Figure 14

ACCEPTED MANUSCRIPT
Physics of Plasmas
This is the author's peer reviewed, accepted manuscript. However, the online version of record will be different from this version once it has been copyedited and typeset.
PLEASE CITE THIS ARTICLE AS DOI: 10.1063/1.5097143
AIP Publishing

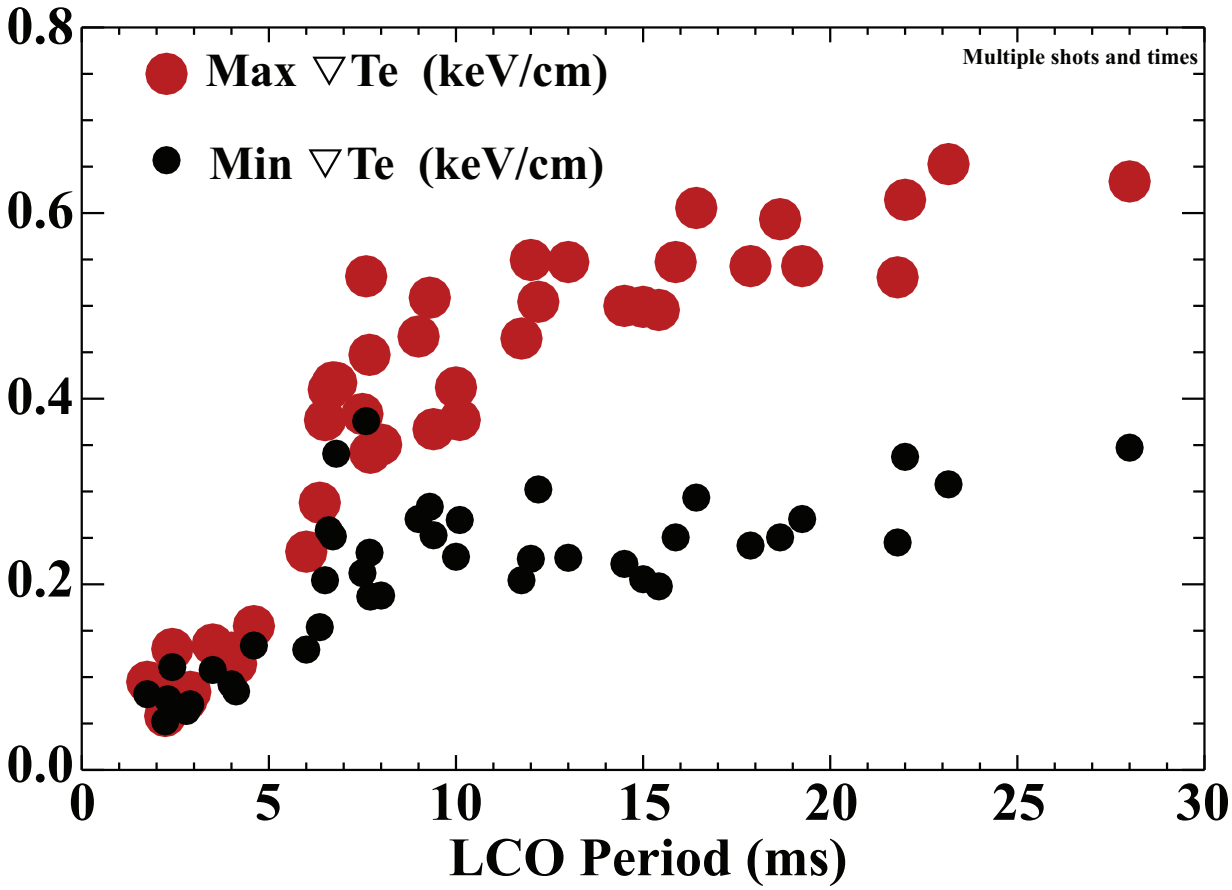

Figure 15